(12) INTERNATIONAL APPLICATION PUBLISHED UNDER THE PATENT COOPERATION TREATY (PCT)

(19) World Intellectual Property Organization
International Bureau

(43) International Publication Date
19 October 2023 (19.10.2023)

WIPO | PCT

(10) International Publication Number
WO 2023/201183 A1

(51) International Patent Classification:
D04H 3/015 (2012.01) *D01C 3/00* (2006.01)
D01D 5/00 (2006.01) *D04H 3/16* (2006.01)
D01B 7/02 (2006.01)

(21) International Application Number:
PCT/US2023/065431

(22) International Filing Date:
06 April 2023 (06.04.2023)

(25) Filing Language: English

(26) Publication Language: English

(30) Priority Data:
63/331,323 15 April 2022 (15.04.2022) US

(71) Applicant: **UNM RAINFOREST INNOVATIONS** [US/US]; Lobo Rainforest Bldg., 101 Broadway Blvd. NE, Suite 1100, Albuquerque, NM 87102 (US).

(72) Inventors: **HAN, Sang, Eon**; C/o Unm Rainforest Innovations, 101 Broadway Blvd. NE, Suite 1100, Albuquerque, NM 87102 (US). **HAN, Sang, M.**; C/o Unm Rainforest Innovations, 101 Broadway Blvd. NE, Suite 1100, Albuquerque, NM 87102 (US). **PARK, Bokyung**; C/o Unm Rainforest Innovations, 101 Broadway Blvd. NE, Suite 1100, Albuquerque, NM 87102 (US).

(74) Agent: **HSIEH, Timothy, M.**; Mh2 Technology Law Group LLP, 1951 Kidwell Drive, Suite 310, Tysons Corner, VA 22182 (US).

(81) Designated States *(unless otherwise indicated, for every kind of national protection available)*: AE, AG, AL, AM, AO, AT, AU, AZ, BA, BB, BG, BH, BN, BR, BW, BY, BZ,

(54) Title: WELL-CONTROLLED ELECTROSPUN NANOSTRUCTURES AND METHODS THEREOF

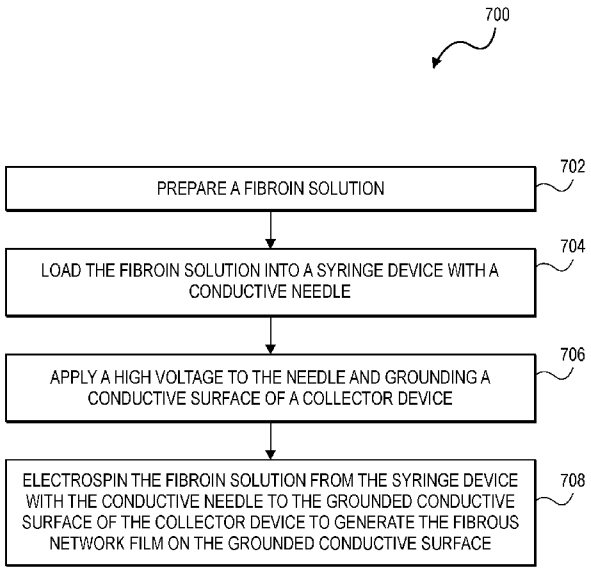

FIG. 7

(57) Abstract: Electrospun films of nonwoven silk nanofibers, when appropriately structured, can surpass Cyphochilus scales in scattering strength for the entire visible spectrum. Detailed modeling studies demonstrate how the key structural parameters affect scattering properties in the electrospun films. An electrospun film with the similar characteristic structural parameters as those in Cyphochilus scales provides two resonance peaks in the visible reflectance spectrum in the limit of a uniform fiber diameter. As the distribution of diameter increases appreciably to experimentally achievable degrees, the resonance peaks broaden and the reflectance spectrum becomes relatively flat with stronger scattering in shorter wavelengths, resulting in disappearance of the structural color. This supports the concept that controllable fibrous nanostructures that exceed the exceptionally strong broadband optical scattering found among living organisms can be volume-produced.

WO 2023/201183 A1

[Continued on next page]

CA, CH, CL, CN, CO, CR, CU, CV, CZ, DE, DJ, DK, DM, DO, DZ, EC, EE, EG, ES, FI, GB, GD, GE, GH, GM, GT, HN, HR, HU, ID, IL, IN, IQ, IR, IS, IT, JM, JO, JP, KE, KG, KH, KN, KP, KR, KW, KZ, LA, LC, LK, LR, LS, LU, LY, MA, MD, MG, MK, MN, MU, MW, MX, MY, MZ, NA, NG, NI, NO, NZ, OM, PA, PE, PG, PH, PL, PT, QA, RO, RS, RU, RW, SA, SC, SD, SE, SG, SK, SL, ST, SV, SY, TH, TJ, TM, TN, TR, TT, TZ, UA, UG, US, UZ, VC, VN, WS, ZA, ZM, ZW.

(84) **Designated States** *(unless otherwise indicated, for every kind of regional protection available)*: ARIPO (BW, CV, GH, GM, KE, LR, LS, MW, MZ, NA, RW, SC, SD, SL, ST, SZ, TZ, UG, ZM, ZW), Eurasian (AM, AZ, BY, KG, KZ, RU, TJ, TM), European (AL, AT, BE, BG, CH, CY, CZ, DE, DK, EE, ES, FI, FR, GB, GR, HR, HU, IE, IS, IT, LT, LU, LV, MC, ME, MK, MT, NL, NO, PL, PT, RO, RS, SE, SI, SK, SM, TR), OAPI (BF, BJ, CF, CG, CI, CM, GA, GN, GQ, GW, KM, ML, MR, NE, SN, TD, TG).

Published:

— *with international search report (Art. 21(3))*

WELL-CONTROLLED ELECTROSPUN NANOSTRUCTURES AND METHODS THEREOF

REFERENCE TO RELATED APPLICATIONS

[0001] This international application claims the benefit of U.S. Provisional Patent Application No. 63/331,323, filed on April 15, 2022, which is hereby incorporated by reference in its entirety.

STATEMENT OF GOVERNMENT INTEREST

[0002] This invention was made with government support under Grants 1231046 and 1555290 awarded by the National Science Foundation (NSF). The government has certain rights in the invention.

TECHNICAL FIELD

[0003] The present teachings relate generally to fibrous network films and, more particularly, to methods for generating nanostructured fibrous network films.

BACKGROUND

[0004] Visual perception of white color stems from multiple scattering of broadband light in random structures. Such structures are found in diverse organisms including beetles, butterflies, spiders, cuttlefish, squids, and clams. These organisms share common structural features, namely, low-index scatterers of optical length scales are randomly distributed to render white color. However, white beetles can be distinguished from the others by their unique structure. White beetle scales contain an interconnected fibrillar nanostructure, while the other organisms possess structures that are based on particles or compartmentalized units such as spheres, ellipsoids, prisms, and multilayer aggregates. As shown in a photograph of a white beetle genus, *Cyphochilus* in FIG. 1A, the scales of the white beetle genus, *Cyphochilus*, can be magnified to reveal the fibrillar nanostructure, which is strongly anisotropic, as depicted in FIG. 1B, which makes it one of the most efficient light-scattering biological structures known today. The fibrils in the nanostructure are made of a low-index chitin and mostly oriented in transverse directions with near isotropy in the lateral plane. Combined with the anisotropy originating from the fibril orientations, a mean fibril diameter

of ~0.25 mm and a filling fraction of ~31.5% achieve the exceptionally strong optical scattering. Prior studies computationally reconstructed approximations of this nanostructure, using the Cahn-Hilliard equation, descriptor functions, and a branching random walk algorithm to establish the structure-scattering relationship. A rather unrealistic but simple model of suspended spheroid nanoparticles has also been used to elucidate the relationship between structure and function. These studies have revealed that the strong scattering depends on the interplay between key structural parameters such as fiber mean diameter, filling fraction, anisotropy, and regularity.

[0005] While the key structural parameters have been identified in these studies, mass production of such computationally reconstructed structures, especially the anisotropic structures, has been challenging due to their formidable complexity. If one sacrifices anisotropy, which is an important structural parameter for the strong scattering in *Cyphochilus* scales, nanostructures that approximately follow the solutions to the Cahn-Hilliard equation can be obtained by slow phase separation. However, previous studies used kinetically-controlled fast phase separation of polymeric mixtures to create porous nanostructures. In this case, the separation process does not lead to a thermodynamically stable state and produces structures of multiple lengths scales with a large surface-to-volume ratio. The large surface free energy makes the structures less stable against various environmental factors such as temperature variations, chemical exposures, mechanical stresses, and high energy irradiations. In comparison, *Cyphochilus* scales preserve structural regularity with relatively uniform length scales, while not strictly minimizing the surface free energy. Within this context, one of the remaining challenges is how to create strongly scattering anisotropic nanostructures of relatively low surface free energy, such that they share the key structural parameters with *Cyphochilus* scales, using fabrication techniques that are amenable to mass production.

[0006] Therefore, it is desirable to provide a method and structure attainable by mass production that faithfully reproduces the important parameters of naturally occurring *Cyphochilus* scales.

SUMMARY

[0007] The following presents a simplified summary in order to provide a basic understanding of some aspects of one or more embodiments of the present teachings. This summary is not an extensive overview, nor is it intended to identify key or critical elements of the present teachings, nor to delineate the scope of the disclosure. Rather, its primary purpose is merely to present one or more concepts in simplified form as a prelude to the detailed description presented later.

[0008] A method of generating a fibrous network film is disclosed. The method of generating a fibrous network film includes preparing a fibroin solution. The method of

generating a fibrous network film also includes loading the fibroin solution into a syringe with a conductive needle or nozzle. The method of generating a fibrous network film also includes applying a high voltage to the needle or nozzle and grounding a conductive surface of a collector. The method of generating a fibrous network film also includes electrospinning the fibroin solution from the syringe or nozzle with the conductive needle or nozzle to the grounded conductive surface of the collector to generate the fibrous network film on the grounded conductive surface. Implementations of the method of generating a fibrous network film may include where the collector moves in lateral motion relative to the conductive needle during the electrospinning or where the collector is rotated. The conductive needle can be a 21-gauge stainless-steel needle. The collector can be drum-shaped with a diameter of about 1 cm to about 15 cm and the grounded conductive surface may include stainless steel. The collector can be rotated about an axis at of about 20 to about 45 rpm during the electrospinning. A distance between a tip of the conductive needle and the grounded conductive surface can be 15 cm. The high voltage can be approximately 21 kv. Using the regenerated silk fibroin powder to produce the fibroin solution may include dissolving the regenerated silk fibroin powder in 98% formic acid for three hours at a concentration varying from 8 to 15 wt% to produce an unfiltered solution of silk fibroin, and filtering the unfiltered solution of silk fibroin through a polyethylene porous membrane to produce the fibroin solution. The preparing the fibroin solution may include preparing a powder of regenerated silk fibroin, and using the powder of regenerated silk fibroin to produce the fibroin solution. The preparing the powder of regenerated silk fibroin may include removing sericin from white silk cocoons to produce degummed silk cocoons, rinsing the degummed silk cocoons with distilled water at 100c for 150 seconds, further rinsing the rinsed degummed silk cocoons with cold distilled water, drying the further rinsed degummed silk cocoons at 80°C for approximately 24 hours, dissolving the dried silk cocoons at a liquor ratio of 1:20 in a CaCl2/H2O/EtOH (1/8/2 molar ratio) mixture solvent at 85°C for approximately 30 minutes to produce a silk fibroin solution, placing the silk fibroin solution in a tube of a cellulose membrane and dialyzing the silk fibroin solution for 4 days by circulating distilled water around the tube, filtering the dialyzed silk fibroin solution through a polyethylene porous membrane to produce a filtered solution of regenerated silk fibroin, drying the filtered solution of regenerated silk fibroin, and grinding the dried, regenerated silk fibroin into the powder of regenerated silk fibroin. Removing sericin from white silk cocoons to produce degummed silk cocoons may include preparing an aqueous solution of 0.2% w/v sodium carbonate and 0.3% w/v sodium oleate; heating the aqueous solution to 105°C, and heating the white silk cocoons in the aqueous solution for approximately 90 minutes to produce the degummed silk cocoons. The white silk cocoons can be Bombyx Mori (geumokjam) white silk cocoons. The cold distilled water can be distilled water at approximately 10°C. The

fibrous network film generated by any of the method can include where the electrospinning the fibroin solution from the syringe with the conductive needle to the grounded conductive surface of the collector to generate the fibrous network film on the grounded conductive surface may include generating a plurality of electrospun fibers, where each of the plurality of electrospun fibers exhibits a fiber diameter value as a function of fiber length such that a relative standard deviation σ of fiber diameter values for each of the plurality of electrospun fibers is approximately 0.32, the plurality of electrospun fibers, taken together, exhibit a mean fiber diameter value that is one of approximately 0.30 μm and approximately 0.32 μm, and the plurality of electrospun fibers in the fibrous network film exhibit a filling fraction from approximately 10% to approximately 60%. The filling fraction can be between approximately 31% and approximately 45%. The mean fiber diameter value is approximately 0.32 μm and the filling fraction is approximately 38%. The filling fraction can be between approximately 31% and approximately 45%. An index of refraction of the fibrous network film can be from about 1.4 to about 1.6. In examples, electrospinning the fibroin solution from the syringe with the conductive needle to the grounded conductive surface of the collector to generate the fibrous network film on the grounded conductive surface may include generating a plurality of electrospun fibers, where each of the plurality of electrospun fibers exhibits a fiber diameter value as a function of fiber length such that a relative standard deviation σ of fiber diameter values for each of the plurality of electrospun fibers is approximately 0.35, the plurality of electrospun fibers, taken together, exhibit a mean fiber diameter value that is approximately 0.20 μm, and the plurality of electrospun fibers in the fibrous network film exhibit a filling fraction from approximately 10% to approximately 60%. Implementations can include an optical film that can include the fibrous network film. Implementations can include a clothing item that can include the fibrous network film.

[0009] A method of generating a fibrous network film is disclosed. The method of generating a fibrous network film includes preparing a polymer solution. The method of generating a fibrous network film also includes loading the polymer solution into a syringe with a conductive needle or nozzle, applying a high voltage to the needle and grounding a conductive surface of a collector, electrospinning the polymer solution from the syringe with the conductive needle to the grounded conductive surface of the collector to generate the fibrous network film on the grounded conductive surface, and where an index of refraction of the fibrous network film can be from about 1.4 to about 1.6, and the fibrous network film may include a plurality of electrospun polymer fibers.

[0010] A fibrous network film can include of a plurality of electrospun fibers. The fibrous network film can also include where each of the plurality of electrospun fibers exhibits a fiber diameter value as a function of fiber length such that a relative standard deviation σ of fiber diameter values for each of the plurality of electrospun fibers is approximately 0.32, the

plurality of electrospun fibers, taken together, exhibit a mean fiber diameter value that is one of: approximately 0.30 μm and approximately 0.32 μm, and the plurality of electrospun fibers in the fibrous network film exhibit a filling fraction from approximately 10% to approximately 60%. Implementations may include where the filling fraction is between approximately 31% and approximately 45%. The mean fiber diameter value is approximately 0.32 μm and the filling fraction is approximately 38%.

[0011] A fibrous network film may include of a plurality of electrospun fibers. The fibrous network film can include where each of the plurality of electrospun fibers exhibits a fiber diameter value as a function of fiber length such that a relative standard deviation σ of fiber diameter values for each of the plurality of electrospun fibers is approximately 0.35, the plurality of electrospun fibers, taken together, exhibit a mean fiber diameter value that is approximately 0.20 μm, and the plurality of electrospun fibers in the fibrous network film exhibit a filling fraction from approximately 10% to approximately 60%. The fibrous network film can include where the filling fraction is between approximately 31% and approximately 45%.

[0012] The features, functions, and advantages that have been discussed can be achieved independently in various implementations or can be combined in yet other implementations further details of which can be seen with reference to the following description.

BRIEF DESCRIPTION OF THE DRAWINGS

[0013] The accompanying drawings, which are incorporated in and constitute a part of this specification, illustrate embodiments of the present teachings and together with the description, serve to explain the principles of the disclosure. In the FIG.s:

[0014] FIGS. 1A and 1B are photographs of a *Cyphochilus* white beetle and an SEM image of a cross-section of its scale, respectively, in accordance to the present disclosure.

[0015] FIG. 2A is a schematic of an effective medium model for fibrous random media.

[0016] FIG. 2B is a plot depicting a calculated phase function at $\lambda = 0.555$ μm.

[0017] FIG. 2C is a plot depicting effective transport mean free path ($L_{zz}^{*\prime}$) spectra for anisotropic (random orientation only in the plane perpendicular to the incident light) and isotropic (random orientation in all directions) fibrous media for the same key structural parameters (except anisotropy) and the refractive index of the fibers as those in *Cyphochilus* scales.

[0018] FIGS. 3A and 3B depict angular intensity distribution of light transmitted through an electrospun film and scattered into air (FIG. 3A) and borosilicate glass (FIG. 3B), obtained

from experiment and solutions to RTE, at l = 0.654 mm, using a mean fiber diameter of d_0 = 0.20 mm and filling fraction of f = 19.6 %, in accordance with the present disclosure.

[0019] FIG. 4A is a composite SEM image of top and cross-sectional views of an electrospun silk film.

[0020] FIG. 4B is a plot depicting light scattering strength as a function of silk filling fraction and mean fiber diameter at $\lambda = 0.555$ μm when $\sigma = 0.49$ as in *Cyphochilus* scales.

[0021] FIG. 4C is a plot depicting effective transport mean free path ($L_{zz}^{*\prime}$) as a function of filling fraction for $d_0 = 0.20$ μm and $\lambda = 0.654$ μm obtained by experiment and model calculation.

[0022] FIG. 4D is a plot depicting effective transport mean free path ($L_{zz}^{*\prime}$) as a function of filling fraction for $d_0 = 0.30$ μm at $\lambda = 0.654$ μm obtained by experiment and model calculation.

[0023] FIG. 4E is a plot depicting effective transport mean free path ($L_{zz}^{*\prime}$) spectra obtained by model calculation.

[0024] FIG. 4F is a plot depicting effective transport mean free path ($L_{zz}^{*\prime}$) spectra obtained experimentally.

[0025] FIG. 5A is a plot depicting Effective transport mean free path ($L_{zz}^{*\prime}$) as a function of filling fraction for electrospun silk structures of $d_0 = 0.30$ μm at $\lambda = 0.900$ μm obtained by experiment and model calculation, with the model calculation assuming experimentally determined σ.

[0026] FIG. 5B is a plot depicting an average cosine of scattering angle $\langle \cos\theta \rangle$ as a function of the cosine of incident angle $\cos\theta'$ for a scattering unit of *Cyphochilus* scales as compared to the model, where the model calculation assumed the same d_0, f, σ, and refractive index as those in naturally occurring *Cyphochilus* scales.

[0027] FIGS. 6A – 6C depict the effect on $\langle \cos\theta \rangle$, Q_{sca}, and $d_0/L_{zz}^{*\prime}$ of mean fiber diameter and fiber diameter distribution on the scattering properties at a visible wavelength λ = 0.900 μm and f = 31.5%.

[0028] FIGS. 6D – 6F depict the effect on $\langle \cos\theta \rangle$, Q_{sca}, and $d_0/L_{zz}^{*\prime}$ of mean diameter and diameter distribution on the scattering properties at a visible wavelength λ = 0.555 μm and f = 31.5%.

[0029] FIGS. 6G and 6H depict an electric energy density map for a cross-section of in the fibers for light incident in the z-direction, corresponding to $d = 0.20$ μm and 0.34 μm, respectively.

[0030] FIG. 6I is a plot depicting reflectivity as a function of wavelength for a purple structural color 600 transitioning to a whiter color 602 as σ becomes larger.

[0031] FIG. 7 is a flow chart illustrating a method of generating a fibrous network film, in accordance with the present disclosure.

[0032] It should be noted that some details of the FIG.s have been simplified and are drawn to facilitate understanding of the present teachings rather than to maintain strict structural accuracy, detail, and scale.

DETAILED DESCRIPTION

[0033] Reference will now be made in detail to exemplary embodiments of the present teachings, examples of which are illustrated in the accompanying drawings. Wherever possible, the same reference numbers will be used throughout the drawings to refer to the same, similar, or like parts.

[0034] The challenge of creating strongly scattering anisotropic nanostructures of relatively low surface free energy, such that they share the key structural parameters with naturally occurring *Cyphochilus* scales, using fabrication techniques that are amenable to mass production leads to a need for a method and structure attainable by mass production that faithfully reproduces these important structural parameters.

[0035] As described herein, *Cyphochilus* white beetles present one of the strongest optical scattering materials in nature. However, the intricate optical fibrillar network nanostructure inside the scales has been difficult to mimic without using complicated templating techniques. In the present teachings, characteristic structural parameters inside *Cyphochilus* scales – mean fiber diameter, diameter distribution, filling fraction, and structural anisotropy – are replicated in synthetic nanofibrous materials to functionally mimic the biological material. To fabricate the synthetic nanostructure, electrospinning is used because this conventional technique is amenable to nanomanufacturing and scale up. The present teachings provide a method including electrospinning, a well-established technique for mass production of nanoscale fibers, used in the creation of highly anisotropic fibrous networks where fiber diameter is relatively uniform around a quarter micrometer and filling fraction is near 30-40%, in agreement with those in *Cyphochilus* scales. Compared to the phase separation techniques, the electrospinning method enables precise control of the nanostructural parameters. In the method and structures provided in the present teachings, it is expected that the exceptionally strong scattering can be achieved in an electrospun structure by replicating the key structural parameters found in *Cyphochilus* scales. To maximize scattering strength in the electrospun nanofibers, optical modeling is performed based on effective medium theory and the structural parameters are optimized by modeling calculations. The optimized parameters in electrospun structures are found to be only slightly different from those in *Cyphochilus* scales. At the optimum, electrospun structures exhibit even stronger optical scattering than

Cyphochilus scales, as confirmed by experimental measurements that match well with modeling calculations.

[0036] The present teachings reveal that electrospun films of nonwoven silk nanofibers, when appropriately structured, can surpass *Cyphochilus* scales in scattering strength for the entire visible spectrum. Furthermore, the detailed modeling study disclosed herein demonstrates how the key structural parameters affect scattering properties in the electrospun films. An electrospun film with the similar characteristic structural parameters as those in *Cyphochilus* scales gives two resonance peaks in the visible reflectance spectrum in the limit of a uniform fiber diameter. The stronger resonance is located in the blue and the weaker resonance in the red, giving a purple structural color. As the distribution of diameter increases appreciably to experimentally achievable degrees, the resonance peaks broaden and the reflectance spectrum becomes relatively flat with stronger scattering in shorter wavelengths, resulting in disappearance of the structural color. These results support that controllable fibrous nanostructures that exceed the exceptionally strong broadband optical scattering found among living organisms can be volume-produced. This detailed investigation, as well as optimization, can be facilitated by the fact that, in comparison to highly irregular structures in previous studies, electrospun structures are simple such that their optical modeling is straightforward. Even in cases where the optical scattering in electrospun structures may not be sufficiently strong since the fibers are much longer than their diameter, these long fibers support mostly 2-dimentional (2D) scattering which is known to be weak as manifested by a strong peak in the forward direction in the phase function.

Optical Modeling

[0037] Based on the high length-to-diameter aspect ratio and low curvature of electrospun fibers, the dimensions of the electrospun fibers can be approximated as a collection of infinitely long cylinders to model their optical properties. In the limit of negligible interaction between the cylinders, the Mie solutions for single cylinders can be used to predict the optical properties of the media. For dense fibrous media, the optical behavior becomes complicated due to interactions between the cylinders. Furthermore, as the cylinder diameter increases toward optical wavelengths, resonant modes tend to spread out of the cylinder, increasing and complicating the interactions. In the approach taken in the present teachings, weak interactions are assumed, so that the distant region surrounding the cylinder is regarded as being occupied by a uniform medium with an effective refractive index represented by the Maxwell-Garnett mixing rule.

[0038] FIG. 2A is a schematic of an effective medium model for fibrous random media. FIG. 2B is a plot depicting a calculated phase function at $\lambda = 0.555$ μm. FIG. 2C is a plot depicting effective transport mean free path ($L_{zz}^{*\prime}$) spectra for anisotropic (random orientation only in

the plane perpendicular to the incident light) and isotropic (random orientation in all directions) fibrous media for the same key structural parameters (except anisotropy) and the refractive index of the fibers as those in *Cyphochilus* scales. In C), $L_{zz}^{*\prime}$ for *Cyphochilus* scales adapted from literature is shown for comparison. In FIG. 2C, $L_{zz}^{*\prime}$ for *Cyphochilus* scales adapted from literature is shown for comparison.

[0039] An effective medium model for a fibrous random media is shown in FIG. 2A. For a medium filling fraction f, a cylinder representing a fiber 200 with a diameter d is assumed to be surrounded by a concentric air cylinder 202 with a diameter $d/\sqrt{f}$ so that the filling fraction in the space occupied by the two concentric cylinders 200, 202 is f [FIG. 2(A)]. The region outside the air cylinder is treated as an effective medium 204. The Mie solutions for the concentric cylinders 200, 202 in an effective medium 204 are integrated over their orientations and diameter distributions to give the scattering cross section and the phase function. A more accurate model, while not used in the present disclosure, can also be used where the effective index is determined self-consistently by imposing a condition that an average optical energy density in the two concentric cylinders 200, 202 is the same as that in the effective medium 204. The z-axis 206 is indicative of the incident light propagation.

[0040] FIG. 2B is a plot depicting a calculated phase function at wavelength $\lambda = 0.555$ μm. Optical scattering in dense electrospun fibrous media can be calculated following a radiative transfer approach. In this approach, the scattering cross section and the phase function are used in the radiative transfer equation (RTE) to calculate specific intensity as a function of spatial position and direction. RTE can be simplified into the diffusion equation when the angular dependence of specific intensity is assumed to be small. FIG. 2C depicts an effective transport mean free path ($L_{zz}^{*\prime}$) spectra for anisotropic (random orientation only in the plane perpendicular to the incident light) and isotropic (random orientation in all directions) fibrous media for the same key structural parameters. In the diffusion approximation, for a lossless anisotropic medium, transmissivity and reflectivity of a thick film for normal incidence are determined by a single characteristic length. This length is called the effective transport mean free path $L_{zz}^{*\prime}$, which is the vertical thickness direction component (zz) of its tensorial form $\mathcal{L}^{*\prime}$. $L_{zz}^{*\prime}$ is the z-length over which the direction of light propagation becomes randomized, so that $1/L_{zz}^{*\prime}$ represents scattering strength in the z-direction. The assumption of small angular dependence for the diffusion approximation can be problematic for fibrous media because of their strongly forward-scattering nature. Nevertheless, transmissivity and reflectivity for electrospun media are calculated with negligible errors by the diffusion model. Thus, the expression $1/L_{zz}^{*\prime}$ is used to characterize the scattering strength of electrospun films but RTE is solved to calculate angular dependence of their transmitted intensity.

[0041] A collection of infinitely long cylinders supports mostly 2D scattering. Because the phase function for the 2D scattering is in general strongly peaked in the forward direction, electrospun structures might result in only weak scattering. On an opposite side, an advantageous point for electrospun structures may be that the fibers are oriented mostly in the transverse directions, so that the orientation-induced anisotropy can be exploited for strong optical scattering. Previous studies have shown that optical scattering in *Cyphochilus* scales may be enhanced by increasing the anisotropy of the nanostructure. However, it is not clear whether the same property would hold true for a medium of long fibers. Thus, it has been tested using modeling calculations to determine how optical scattering is affected by the anisotropy and how strong the 2D scattering in electrospun structures is in comparison to that in *Cyphochilus* scales.

[0042] FIG. 2B depicts a plot of calculated phase functions at a wavelength of $\lambda = 0.555$ μm for both isotropic and anisotropic electrospun structures that have the same refractive index, filling fraction, and diameter distribution as those in *Cyphochilus* scales. The fibers are randomly oriented over all directions in the isotropic structure, whereas they are oriented only in transverse directions in the anisotropic structure. For the anisotropic structure, the phase function is for normal incidence. Forward scattering near the scattering angle of $\theta = 0°$ is strong [note that a logarithm is taken of the phase function in FIG. 2B] for both structures but, for the anisotropic structure, backward scattering is also significant. Accordingly, the phase function in the anisotropic structure contributes to increasing scattering strength or decreasing ${L_{zz}}^{*\prime}$ compared to that in the isotropic structure. FIG. 2C shows that this behavior is maintained throughout the visible spectrum. Interestingly, ${L_{zz}}^{*\prime}$ in the *Cyphochilus* structure is located between ${L_{zz}}^{*\prime}$'s of the two structures. This is reminiscent of a previous study where it is argued that, in the biological structure, scattering would become stronger as its anisotropy increases. The anisotropic structure considered in FIG. 2B and FIG. 2C has the maximum desired anisotropy among rotationally symmetric random fibrous structures because its fibers are oriented strictly in the transverse directions. In addition, the spectral dependence of ${L_{zz}}^{*\prime}$ for the electrospun structures is similar to that for *Cyphochilus* scales, as ${L_{zz}}^{*\prime}$ increases as λ increases for all structures considered in FIGS. 2A – 2C. Therefore, the modeling demonstrates that anisotropic electrospun structures (solid line in FIG. 2C) may be able to achieve even stronger scattering than *Cyphochilus* scales throughout the visible spectrum, provided that the model for maximized anisotropy accurately represents optical behavior of experimental structures and that electrospinning of materials of similar refractive index to chitin can achieve the structural parameters used in the calculations. These two points are addressed further herein.

Model Validation and Optical Characterization of Electrospun Films

[0043] FIGS. 3A and 3B depict angular intensity distribution of light transmitted through an electrospun film and scattered into air (FIG. 3A) and borosilicate glass(FIG. 3B), obtained from experiment and solutions to RTE, at l = 0.654 mm, using a mean fiber diameter of d_0 = 0.20 mm and filling fraction of f = 19.6 %.

[0044] To test whether the modeling described in regard to FIGS. 2A – 2C, can reproduce experimental results, angular dependence of transmitted light was examined. For experimental examination, two electrospun silk samples were produced: a free-standing electrospun fibrous film (300 FIG. 3A inset) and a fibrous coating 304 on a 150-μm-thick borosilicate glass slide 306, as shown in example 302, FIG. 3B inset. The angular distribution of transmitted light intensity at normal incidence of a He-Ne laser at λ = 0.654 μm was measured for the two samples and compared with predictions by RTE for fibers oriented only in transverse directions. For the coating sample, the transmitted light emerged from the glass slide. To eliminate Fresnel refraction from the bottom surface of the slide, a hemispherical borosilicate glass (N-BK7 Half-Ball Lens, Edmund Optics) was glued to the slide surface with an index matching gel 308. For both samples, a mean fiber diameter of d_0 = 0.20 μm and a filling fraction of f = 19.6 % with a film/coating thickness of 26 μm were chosen. FIGS. 3A and 3B show $P(\mu_e)/\mu_e$ for the free-standing and coating samples, respectively, where P is the transmitted light power and $\cos^{-1}\mu_e$ is the angle from the normal as the light exits the samples. $P(\mu_e)$ is normalized by $\int_0^1 P(\mu_e)d\mu_e = 1$ and $P(\mu_e)/\mu_e$ becomes 2 for a Lambertian surface. In general, the calculated $P(\mu_e)/\mu_e$ spectra match well with experiments. The exact reasons for small deviations between the two are difficult to identify. However, a likely reason is that the model is limited in describing optical scattering at interfaces, as it assumes a unit in FIG. 2A derived from bulk structures and the fibers near interfaces have a different environment from the bulk. In addition, the calculated curve exhibits a sharp feature near μ_e = 0.68 in FIG. 3B because Fresnel's law is assumed for internal reflection. The smooth experimental response near μ_e = 0.68 can be better described by an improved model such as some previously developed. Outside these minor subtleties at the interfaces, however, the current model can predict properties in the bulk, such as ${L_{zz}}^{*\prime}$, with better accuracy than those that are directly affected by the interfaces. It will be shown and described later that the model calculations of ${L_{zz}}^{*\prime}$ spectrua match well with experiments on electrospun structures.

[0045] FIG. 4A is a composite SEM image of top and cross-sectional views of an electrospun silk film. FIG. 4B is a plot depicting light scattering strength as a function of silk filling fraction and mean fiber diameter at λ = 0.555 μm when σ = 0.49 as in *Cyphochilus* scales. FIG. 4C is a plot depicting effective transport mean free path (${L_{zz}}^{*\prime}$) as a function of

filling fraction for $d_0 = 0.20$ μm and $\lambda = 0.654$ μm obtained by experiment and model calculation. FIG. 4D is a plot depicting effective transport mean free path ($L_{zz}^{*\prime}$) as a function of filling fraction for $d_0 = 0.30$ μm at $\lambda = 0.654$ μm obtained by experiment and model calculation. FIG. 4E is a plot depicting effective transport mean free path ($L_{zz}^{*\prime}$) spectra obtained by model calculation. FIG. 4F is a plot depicting effective transport mean free path ($L_{zz}^{*\prime}$) spectra obtained experimentally. In FIGS. 4E and 4F, $L_{zz}^{*\prime}$ for *Cyphochilus* scales adapted from literature values is presented for comparison. In FIGS. 4C – 4F, the model calculation assumed experimentally determined σ.

[0046] To evaluate how closely the key structural parameters of *Cyphochilus* scales, for example, (i) anisotropy, (ii) fiber mean diameter, (iii) regularity, and (iv) filling fraction, can be realized in electrospun structures, images of electrospun fibers obtained by scanning electron microscopy (SEM) were analyzed and measured for density of the structures. (i) SEM images of top and cross section shown in in FIG. 4A demonstrate that the fibers are randomly oriented mostly in the transverse plane, yet parallel with the surface plane, such that the anisotropy is strong. These long strands of silk fibers are laid down in the plane of deposition, randomly distributed, and present as a layer by layer structure. (ii) The fiber mean diameter, d_0, varies approximately from 0.20 to 0.30 mm in the experimental conditions of the present disclosure. These experimental values, as well as the mean diameter in *Cyphochilus* scales (d_0 = 0.25 μm) is also depicted in the plot of FIG. 4B. (iii) Regularity is defined herein as a structural property represented by diameter uniformity and surface smoothness of the fibers. The diameter varies minimally along the fiber axis and the fiber surface is smooth. The diameter distribution has a relative standard deviation of σ = 0.32 – 0.35, which is narrower than that (σ = 0.49) in *Cyphochilus* scales as found in nature. It follows from the observations that, according to the definition of regularity, the electrospun structures of the present disclosure provide a more regular structure as compared to the structure in the beetle scales. (iv) Matching the filling fraction observed in *Cyphochilus* scales (f = 31.5%) is not trivial, since electrospinning typically produces fibrous structures with a low filling fraction. To overcome this difficulty, the collector size can be decreased in the electrospinning system, which greatly increased the filling fraction approximately from 10% to 60%. As the filling fraction was varied by changing the collector size, the fiber mean diameter d_0 remained fairly constant. For the d_0's tested in the present teachings, the variation in d_0 upon filling fraction change is 0.20 ± 0.01 μm and 0.30 ± 0.02 μm. It should be noted that filing fraction % is similar to and can be considered as essentially an inverse of porosity. The filling fraction percent can be defined as a ratio of unoccupied volume to occupied volume. The filling fraction is typically measured by volume displacement. Where density differences are present, the density of different solvents can be utilized to determine

filling fractions or porosity. While decreasing the collector size influenced filling fraction, it should be noted that reducing the filling fraction can be achieved by other means known to those skilled in the art in alternate examples, such as varying solvent properties, polymer properties, processing additives, flow rate, voltage applied, nozzle size or needle gauge, distance from tip to collector, and the like. In certain examples, a needle-less dispensing system may be utilized. Furthermore, ambient temperature and humidity can modify the porosity as well, as these parameters are known to influence the fiber diameter, density, and therefore the porosity.

[0047] Among the key parameters, anisotropy and diameter distribution are not easily controlled in electrospinning. Thus, for structural optimization using the model, only fiber mean diameter and filling fraction were varied with a fixed normal diameter distribution at σ = 0.49 as in *Cyphochilus* scales. FIG. 4B shows scattering strength, $1/L_{zz}^{*\prime}$ as a function of d_0 and f at λ = 0.555 μm, where the human eye is most sensitive under daylight. The optimum point over 0.1 μm $\leq d_0 \leq$ 0.4 μm and 10% $\leq f \leq$ 60% is determined to be d_0 = 0.32 μm and f = 38%, which are slightly different from those in *Cyphochilus* scales (d_0 = 0.25 μm and f = 31.5%). The optimum f is located roughly in the middle because the density of scattering centers vanishes as f approaches 0 or 100%. Having found the rough estimates of the optimum parameters in FIG. 4(B), electrospinning conditions were established to obtain samples with two fiber mean diameters d_0 = 0.20 μm and 0.30 μm with filling fractions varying from 10% to 60 %. To extract $L_{zz}^{*\prime}$ from the samples, linear regression on plots of inverse transmissivity vs. film thickness was performed. FIGS. 4C and 4D show that, at a He-Ne laser wavelength of 0.654 μm, $L_{zz}^{*\prime}$ is minimized at f = 26% and 40% for d_0 = 0.20 μm and 0.30 μm, respectively. These optimum f values are close to the predictions of 30% and 38% at the same d_0's shown in FIG. 4B. In fact, when actual diameter distributions are considered in the present model, the $L_{zz}^{*\prime}$ curves exhibit a good match between experiment and calculation, which is depicted in the plots of FIG. 4C and 4D. $L_{zz}^{*\prime}$ spectra at the optimum f values for calculation and experiment are shown in FIGS. 4E and 4F, respectively. The calculation and experiment match reasonably well with each other, with the experimental values providing slightly shorter $L_{zz}^{*\prime}$ as compared to the model calculations.

[0048] As evidenced by lower $L_{zz}^{*\prime}$ curves in FIG. 4F the electrospun structures of the present examples outperform *Cyphochilus* scales in optical scattering. Specifically, $L_{zz}^{*\prime}$ is approximately 0.9 μm – 2.1 μm for the two electrospun structures in FIG. 4F, whereas it is 1.5 μm – 2.4 μm for *Cyphochilus* scales in the visible spectrum. Thus, the enhancement factor in the scattering strength by electrospun fibers from *Cyphochilus* scales is 1.1 – 1.7 in the visible spectrum. For all the structures, $L_{zz}^{*\prime}$ increases with λ. Because the refractive indices of silk (1.54 – 1.58) and chitin (1.54 – 1.57) are negligibly different from each other over the

visible spectrum, the stronger scattering of electrospun silk can be considered a structural effect. This result is notable when one considers that only a small number of key structural parameters have been matched to those of *Cyphochilus* scales and that the visual queue of anisotropy was only qualitatively mimicked or reproduced. More importantly, the result demonstrates that a mass-producible nonwoven fabric can exceed the exceptionally strong scattering observed in nature.

Scattering Characteristics

[0049] FIG. 5A is a plot depicting Effective transport mean free path ($L_{zz}^{*\prime}$) as a function of filling fraction for electrospun silk structures of $d_0 = 0.30$ μm at $\lambda = 0.900$ μm obtained by experiment and model calculation, with the model calculation assuming experimentally determined σ. FIG. 5B is a plot depicting an average cosine of scattering angle $\langle \cos\theta \rangle$ as a function of the cosine of incident angle $\cos\theta'$ for a scattering unit of *Cyphochilus* scales as compared to the model, where the model calculation assumed the same d_0, f, σ, and refractive index as those in naturally occurring *Cyphochilus* scales. The FIG. 5B, inset further depicts a definition of θ and θ'. For a given surface 500, a normal incident angle, z 502 is shown, with an incoming variable incident angle, θ' 504 and the outgoing, scattered angle, θ 506 in relation to the oriented plane of the surface 500. As the structure in an electrospun film is quite different from that in *Cyphochilus* scales, its scattering characteristics may also be different, despite similar magnitudes and spectral dependence in $L_{zz}^{*\prime}$. Scattering characteristics in an electrospun film can be investigated using our model based on infinitely long cylinders. In this case, the scattering characteristics can be represented by the differential scattering cross section, which gives the angular distribution of scattered intensity. However, this quantity is not trivial to obtain for the structure in *Cyphochilus* scales. At the minimum, a scattering unit has to be defined for such intricate continuous structure to determine this quantity. A method to define a scattering unit in the structure within the diffusion theory uses, instead of the differential scattering cross section, average cosine of the polar angles (θ) of the scattered light, $\langle \cos\theta \rangle$, was calculated at $\lambda = 0.900$ μm for varying incident directions represented by $\cos\theta'$ where θ' is the incidence polar angle from the normal. Thus, values were obtained $\langle \cos\theta \rangle(\theta')$ for electrospun structures with the strongest scattering at the same wavelength. This structure was determined based on FIG. 5A, where $L_{zz}^{*\prime}$ as a function of filling fraction at $\lambda = 0.900$ μm shows a good match between experiment and calculation. Based on the model calculation result in FIG. 5A, the electrospun structure with the strongest scattering has $d_0 = 0.30$ μm and $f = 32\%$. At these parameters, $\langle \cos\theta \rangle(\theta')$ was calculated for an electrospun structure and compared with that for *Cyphochilus* scales.

[0050] FIG. 5B shows a comparison between the results on the electrospun structure and the results on *Cyphochilus* scales known in literature. The sign of $\langle \cos\theta \rangle$ determines whether the scattering is overall in the positive or negative z-direction, as depicted in the inset of FIG. 5B. The structures in the electrospun film and *Cyphochilus* scales exhibit different scattering behaviors from each other. Specifically, $\langle \cos\theta \rangle$ remains relatively independent of the incident angle for the electrospun structure, whereas *Cyphochilus* scales exhibit more pronounced dependence. However, both structures overall show $\langle \cos\theta \rangle$ not far from 0 for all incident angles, which would be observed for near isotropic scattering.

[0051] While this feature is notable, it is not clear how individual fibers affect the scattering characteristics since the diameter distribution is rather broad for both structures. Moreover, $\langle \cos\theta \rangle$ does not fully represent $1/{L_{zz}}^{*\prime}$ without being considered in combination with the scattering efficiency Q_{sca}. For example, when $\sigma = 0$ and the zz component of the anisotropy tensor is assumed to be unity, they are related by:

$$\frac{d}{L_{zz}^{*}{}'} = \frac{12f}{\pi}\int_0^1 \left[1 - \frac{\langle \cos\theta \rangle(\theta')}{\cos\theta'}\right] Q_{sca}(\theta')\cos^2\theta' \mathrm{d}(\cos\theta') . \quad (1)$$

[0052] A cursory understanding of how ${d_0}/{L_{zz}}^{*\prime}$ depends on $\langle \cos\theta \rangle$ and Q_{sca} can be obtained by assuming that they are independent of θ'. With this assumption, as we take $\langle \cos\theta \rangle$ and Q_{sca} to be averages over diameter distribution, Eq. (1) is simplified to

$$\frac{d_0}{L_{zz}^{*}{}'} \approx \frac{12f}{\pi} Q_{sca}\left(\frac{1}{3} - \frac{\langle \cos\theta \rangle}{2}\right), \quad (2)$$

[0053] which would be valid only for $\langle \cos\theta \rangle < 2/3$. Approximately, Eq. (2) indicates that scattering strength is directly proportional to Q_{sca} and is reduced as forward scattering ($\langle \cos\theta \rangle$) increases for normal incidence. With the preliminary understanding implied in Eq. (2), an investigation by numerical calculations based on the model show how the diameter distribution and the mean diameter for electrospun structures affect $\langle \cos\theta \rangle$, Q_{sca}, and ${d_0}/{L_{zz}}^{*\prime}$ at normal incidence ($\theta' = 0$).

[0054] FIGS. 6A – 6C depict the effect on $\langle \cos\theta \rangle$, Q_{sca}, and ${d_0}/{L_{zz}}^{*\prime}$ of mean fiber diameter and fiber diameter distribution on the scattering properties at a visible wavelength λ = 0.900 μm and f = 31.5%. FIGS. 6D – 6F depict the effect on $\langle \cos\theta \rangle$, Q_{sca}, and ${d_0}/{L_{zz}}^{*\prime}$ of mean diameter and diameter distribution on the scattering properties at a visible wavelength λ = 0.555 μm and f = 31.5%. FIGS. 6G and 6H depict an electric energy density map for a cross-section of in the fibers for light incident in the z-direction, corresponding to d = 0.20 μm and 0.34 μm, respectively. FIG. 6I is a plot depicting reflectivity as a function of wavelength for a purple structural color 600 transitioning to a whiter color 602 as σ becomes larger. For FIGS. 6A – 6C, a calculated $\langle \cos\theta \rangle$, Q_{sca}, and ${d_0}/{L_{zz}}^{*\prime}$ is displayed as a function

of mean diameter and diameter distribution for $f = 31.5\%$ at $\lambda = 0.900$ μm. FIGS. 6D – 6F) are similar to FIGS. 6A – 6C, but at $\lambda = 0.555$ μm. FIGS. 6G and 6F depict a calculated electric energy density for incident polarization parallel to the fiber axis at $d = 0.20$ μm and 0.34 μm, respectively, corresponding to the two resonances seen in FIG. 6E at $\sigma = 0$. Inner and outer circles represent fiber and air, respectively, as indicated in FIG. 2A. FIG. 6I shows calculated reflectivity spectra of a 10-μm-thick fibrous film for $d_0 = 0.25$ μm and $f = 31.5\%$ at $\sigma = 0$ (solid line) and $\sigma = 0.49$ (dashed line), showing disappearance of a purple structural color when σ is large. The colors shown for the two spectra are those under CIE standard illuminant D65.

[0055] FIGS. 6A – 6C show the results at $\lambda = 0.900$ μm and $f = 31.5\%$ (same as f in *Cyphochilus* scales). In this case, the general trend of $d_0/{L_{zz}}^{*\prime}$ is captured more closely by Q_{sca} than by $\langle \cos\theta \rangle$, also referring to Eq. (2). A resonance appears at $d_0 = 0.33$ μm as $\sigma \to 0$ based on the peak in Q_{sca}, shown in FIG. 6B. The resonance translates to a peak in $d_0/{L_{zz}}^{*\prime}$ as $\sigma \to 0$ at $d_0 = 0.30$ μm, not as clearly seen in FIG. 6C, which is only slightly different from that in Q_{sca}. The resonance peak broadens as the fiber diameter distribution increases.

[0056] The effect of mean diameter and diameter distribution on the scattering properties at a visible wavelength $\lambda = 0.555$ μm and $f = 31.5\%$ is shown in FIGS. 6D – 6F, also in reference to Eq. (2). At this wavelength, $\langle \cos\theta \rangle$, Q_{sca}, and $d_0/{L_{zz}}^{*\prime}$ over 0.1 μm $\leq d_0 \leq$ 0.24 μm are similar to those at $\lambda = 0.900$ μm over 0.16 μm $\leq d_0 \leq$ 0.4 μm, due to scale invariance (d_0/λ = constant) apart from a small refractive index dispersion. Because the wavelength is now shorter, two resonances appear in Q_{sca} at $d_0 \approx 0.20$ μm and 0.34 μm as $\sigma \to 0$ (FIG. 6E). The locations of the resonances are similar to those in $d_0/{L_{zz}}^{*\prime}$ (FIG. 6F). These resonances are also manifested as dips in $\langle \cos\theta \rangle$, the dip at $d_0 \approx 0.20$ μm is sufficiently broad that its positive curvature is not clearly visible in FIG. 6D. As the resonance locations are primarily determined by d_0, similar locations would be obtained when filling fractions are not very different from $f = 31.5\%$.

[0057] In FIG. 6E, the peak in Q_{sca} as $\sigma \to 0$ at $d_0 \approx 0.34$ μm is stronger than that at $d_0 \approx$ 0.20 μm. This is related to electric energy density distribution in the fibers for light incident in the z-direction shown in FIGS. 6G and 6H corresponding to $d = 0.20$ μm and 0.34 μm, respectively. The incident light is polarized with its electric fields parallel to the fiber axis because this polarization dominates the resonances. The resonance at $d = 0.34$ μm supports stronger local electric field in the fiber than the other. As d increases from 0.20 μm to 0.34 μm, resonant modes exhibit a greater number of nodal planes, and interference between the modes and the incident field induces stronger local electric fields. As σ becomes large enough so that σd_0 becomes comparable to half the distance between the two resonance peaks in

FIGS. 6E and 6F, these peaks become sufficiently broadened that they disappear. This broadening is manifested as a color change in the sample.

[0058] For example, the calculated colors based on reflectivity spectra for a 10-μm-thick film in FIG. 6I show that a purple structural color at $\sigma = 0$ tends to disappear when σ increases to 0.49 for $d_0 = 0.25$ μm and $f = 31.5\%$, which are the parameter values for *Cyphochilus* scales. Principle of scale invariance, d/λ = constant, indicates that the resonant modes at $d_0 = 0.20$ μm and 0.34 μm in FIG. 6E would appear near $\lambda = 0.69$ μm and 0.41 μm, respectively, for a uniform diameter of $d = 0.25$ μm. This effect is seen in FIG. 6I as reflectivity peaks at the expected locations when $\sigma = 0$. The stronger peak in FIG. 6F results in a higher reflectivity at $\lambda = 0.41$ μm than at $\lambda = 0.69$ μm in FIG. 6I. When σ is large, these peaks broaden so that reflectivity decreases monotonically as the wavelength increases. For our electrospun structures, σ is 0.32 – 0.35 and, in this range, spectral features in the visible are almost absent in the ${L_{zz}}^{*\prime}$ as shown in FIGS. 4E and 4F. In these spectra, ${L_{zz}}^{*\prime}$ increases as the wavelength increases. The reason for this behavior is that, because ${L_{zz}}^{*\prime}$ is roughly proportional to transmissivity, the wavelength dependence of ${L_{zz}}^{*\prime}$ in the electrospun structures shows an opposite behavior to that of reflectivity shown in FIG. 6I at $\sigma = 0.49$. Furthermore, when diameter distribution is negligible, such as in a single fiber, as shown in FIGS. 6G and 6H, the fiber possesses a structural color. Upon reflection a color is observed, but the color has a a spectral dependence, for example, generating a purple color, as shown in FIG. 6I. As wavelength increases, the color disappears and becomes whiteish with a larger distribution of length scales of fibers.

[0059] The present teachings provide fibrous nanostructures that surpass *Cyphochilus* scales in light scattering strength by focusing on key structural parameters found in the scales, i.e., mean fiber diameter, diameter distribution, filling fraction, and anisotropy. These nanostructures were fabricated by electrospinning, which is amenable to mass production, and scattering characteristics in these structures were investigated by both experiment and optical modeling. Our modeling revealed that, despite large nanostructural difference between *Cyphochilus* scales and electrospun films, the mean diameter and filling fraction at the optimum point for electrospun films are similar to those in *Cyphochilus* scales. With the optimized parameters in electrospun films, their optical scattering is even stronger than that in *Cyphochilus* scales. However, scattering characteristics are different between the two. The detailed modeling study described herein showed two resonance peaks in reflectivity in the limit of uniform-diameter fibers where the diameter matches the mean diameter of *Cyphochilus* scales: a strong and a weak resonance in the blue and red spectral region, respectively. As the fiber diameter becomes more distributed, the resonance peaks broaden and the spectrum becomes relatively flat. Because stronger resonance is located in the blue

spectral region, when the peaks broaden, scattering strength becomes stronger as the wavelength decreases. This spectral dependence is also observed in *Cyphochilus* scales. The present teachings further suggest that well-controlled fibrous nanostructures can be fabricated by conventional manufacturing techniques and optimized for their optical properties by simple optical modeling. To illustrate, control over diameter distribution enables structural color in fibrous media and core-shell fiber structures provide effective control of scattering directions by the Kerker effect. Moreover, fibrous optical films can be flexible with high curvatures for a variety of practical use, unlike other common scattering materials such as paint, optical diffusers, or solid foams. Applications of the present electrospun fibers and films designed according to the present disclosure can have applications in optical films, wound healing films, potentially for use in treating burns, beauty items, patches for outdoor activity that counter sunlight exposure with radiative cooling, delivery packages requiring temperature control for temp sensitive goods, or clothing items having optical radiative cooling properties.

[0060] FIG. 7 is a flow chart illustrating a method of generating a fibrous network film, in accordance with the present disclosure. A method of generating a fibrous network film 700 includes preparing a fibroin solution 702, loading the fibroin solution into a syringe with a conductive needle 704, applying a high voltage to the needle and grounding a conductive surface of a collector 706, and electrospinning the fibroin solution from the syringe with the conductive needle to the grounded conductive surface of the collector to generate the fibrous network film on the grounded conductive surface 708.

[0061] The method of generating a fibrous network film 700 can include the use of a collector that is in motion relative to the conductive needle during the electrospinning, such as, but not limited to lateral motion. In examples, the collector is rotated, moved transversely, moved in one direction or moved in multiple directions in succession. In certain examples, a collector may be a belt or flat substrate moving laterally in a roll-to-roll process. In examples of the method of generating a fibrous network film 700, the conductive needle is a 21-gauge stainless-steel needle, although other sizes of needle are applicable and known to one skilled in the art, provided they are configured to dispense the solution or dispersion used the electrospinning. Certain examples include where the collector is drum-shaped with a diameter of about 1 cm to about 15 cm and the grounded conductive surface comprises stainless steel. In other examples, the grounded conductive surface can be or include other metals or alloys. The collector is rotated about an axis at of about 20 to about 45 rpm during the electrospinning, where a distance between a tip of the conductive needle and the grounded conductive surface is nominally 15 cm. The high voltage used in the method of generating a fibrous network film 700 is approximately 21 kV, although various parameters in the method 700 can influence a suitable high voltage value to be use in the electrospinning process. In

the preparation of the fibroin solution the steps of preparing a powder of regenerated silk fibroin and the use of the powder of regenerated silk fibroin to produce the fibroin solution are employed. Preparing the powder of regenerated silk fibroin can further include removing sericin from white silk cocoons to produce degummed silk cocoons, rinsing the degummed silk cocoons with distilled water at 100°C for 150 seconds, further rinsing the rinsed degummed silk cocoons with cold distilled water, drying the further rinsed degummed silk cocoons at 80°C for approximately 24 hours, dissolving the dried silk cocoons at a liquor ratio of 1:20 in a CaCl2/H2O/EtOH (1/8/2 molar ratio) mixture solvent at 85 °C for approximately 30 minutes to produce a silk fibroin solution, placing the silk fibroin solution in a tube of a cellulose membrane and dialyzing the silk fibroin solution for 4 days by circulating distilled water around the tube, filtering the dialyzed silk fibroin solution through a polyethylene porous membrane to produce a filtered solution of regenerated silk fibroin, drying the filtered solution of regenerated silk fibroin, and grinding the dried, regenerated silk fibroin into the powder of regenerated silk fibroin. Removing sericin from white silk cocoons to produce degummed silk cocoons can include preparing an aqueous solution of 0.2% w/v sodium carbonate and 0.3% w/v sodium oleate, heating the aqueous solution to 105°C, and heating the white silk cocoons in the aqueous solution for approximately 90 minutes to produce the degummed silk cocoons. The cold distilled water can be distilled water at approximately 10°C. Using the regenerated silk fibroin powder to produce the fibroin solution can include dissolving the regenerated silk fibroin powder in 98% formic acid for three hours at a concentration varying from 8 to 15 wt% to produce an unfiltered solution of silk fibroin, and filtering the unfiltered solution of silk fibroin through a polyethylene porous membrane to produce the fibroin solution. In examples, the preparation of silk powders can be employed using silk powders derived from materials including, but not limited to, *Bombyx mori* (Geumokjam) white silk cocoons, or any species of silk cocoons which is mainly comprised of silk fibroin and silk sericin. With the use of alternate silk powder materials, or alternate polymeric starting materials for electrospinning of fibers, alternate reagents may be used in a similar procedure as described previously, such as specific solvents required for dissolution or processing of applicable polymers or reactant materials. In examples, alternate polymeric starting materials can include, but are not limited to, polyesters, polyacrylics, polyamides, and polyethylenes, as well as alginate, chitosan, collagen, fibrinogen, gelatin, hyaluronic acid, cellulose acetate (CA), cellulose triacetate (CTA), polybutylenesuccinate (PBS), nylon, polyacrylonitrile (PAN), polycaprolactone (PCL), polydioxanone (PDO), polyethersulfone (PES), polyethylene oxide (PEO), polyethylene terephthalate (PET), polyglycolic acid (PGA), polyhydroxybutyrate (PHB), polylactic acid (PLA), polylactic-co-glycolic acid (PLGA), poly(lactide-co-caprolactone) (PLCL), polytetrafluoroethylene (PTFE), polyvinyl alcohol (PVA), polyvinylidene fluoride (PVDF), polyvinylpyrrolidone (PVP), polyurethane (PU) and

polystyrene (PS). Another example method of generating a fibrous network film can include the preparation of a polymer solution, loading the polymer solution into a syringe with a conductive needle, applying a high voltage to the needle and grounding a conductive surface of a collector, and electrospinning the polymer solution from the syringe with the conductive needle to the grounded conductive surface of the collector to generate the fibrous network film on the grounded conductive surface, wherein an index of refraction of the fibrous network film is from about 1.4 to about 1.6 and the fibrous network film comprises a plurality of electrospun polymer fibers. In general, polymers having a polymer refractive index around 1.4-1.6, when used make similar electrospun film structures, provide similar performance in terms of optical scattering. In certain examples, the use of different polymers can provide similar scattering strengths, as described herein when fabricated using electrospinning. While a solution preparation may be different for a different polymer, electrospinning can still produce similar structural parameters as described in the present teachings. In addition to other polymer or starting materials described herein, any raw polymer materials having refractive indices in range between about 1.4 to about 1.6 will show similar performance.

[0062] The present teachings provide a fibrous network film consisting of a plurality of electrospun fibers, wherein each of the plurality of electrospun fibers exhibits a fiber diameter value as a function of fiber length such that a relative standard deviation σ of fiber diameter values for each of the plurality of electrospun fibers is approximately 0.32, but ranging from 0 to about 0.6, or from about 0.1 to about 0.5, or from about 0.3 to about 0.4. Furthermore, the plurality of electrospun fibers, taken together, can exhibit a mean fiber diameter value that is one of approximately 0.30 μm and approximately 0.32 μm, ranging from about 0.10 μm to about 0.40 μm, from about 0.25 μm to about 0.35 μm, or from about 0.30 μm to about 0.32 μm. Moreover, the plurality of electrospun fibers in the fibrous network film exhibit a filling fraction from approximately 10% to approximately 60%, from about 10 % to about 50%, or from about 30% to about 45%.

Examples

[0063] Materials and Methods for Electrospinning of Regenerated Silk Fibroin:

[0064] Silk solutions were prepared by our previously reported methods using Bombyx mori (Geumokjam) white cocoons. For electrospinning, the solutions were loaded into a syringe with a 21-gauge stainless steel needle (0.495 mm inner diameter). A high voltage (21 kV) was applied to the tip of the needle and a stainless steel collector was grounded. Distance between the tip and the collector was kept at 15 cm. Filling fraction was controlled by changing the sizes of square-shaped collectors (3, 3.5, 4, 4.5, and 5 cm).

[0065] Example Preparation of Regenerated Silk Fibroin Powder: Silk fibroin powder was derived from *Bombyx mori* (Geumokjam) white silk cocoons after removing sericin by a

process called degumming. Whiteness of the cocoons was determined using CIE 1931 color coordinates as (x, y) = (0.3205, 0.3387) under the CIE Standard lllluminant D_{65}. which were slightly different from the perfect white of (x, y) = (0.3128, 0.3290) under the same illuminant (Figure 58, Supporting Information). For degumming, an aqueous solution of 0.2% w/v sodium carbonate and 0.3% w/v sodium oleate was heated at 105°C. Silk cocoons were heated in the solution for 90 min to ensure almost complete removal of sericin from the cocoons. The weight ratio between the silk cocoons and the aqueous solution (liquor ratio) was 1:25. The degummed silk cocoons, which were comprised mostly of fibroin, were rinsed with distilled water at 100°C for 150 s to remove degumming agents (i.e., sodium carbonate and sodium oleate) and residual sericin from the silk cocoons. After further rinsing with cold distilled water, the silk cocoons were dried at 80°C for a day. To obtain regenerated silk fibroin in a powder form, the degummed silk was dissolved at a liquor ratio of 1:20 in a $CaCl_2/H_20$/EtOH (1/8/2 molar ratio) mixture solvent at 85°C for 30 min. To remove $CaCl_2$ and ethanol from the dissolved silk fibroin, the solution was placed in a tube of a cellulose membrane and was dialyzed for 4 days by circulating distilled water around the tube. The membrane was impenetrable to fibroin of molecular weight over 12,000-14,000. The dialyzed silk fibroin solution was filtered through a polyethylene porous membrane to remove any extraneous dirt. The filtered solution of regenerated silk fibroin was dried and ground into powder.

[0066] Electrospinning of Regenerated Silk Fibroin: Regenerated silk fibroin powder was dissolved in 98% formic acid for 3 h at a concentration varying from 8 to 15 wt% and filtered through a polyethylene porous membrane. The fibroin solution was loaded into a syringe with a 21-gauge stainless steel needle (inner diameter of 0.495 mm) for electrospinning. Next, 22.5 kV was applied to the needle and a 9 cm diameter drum-shaped collector was electrically grounded. The distance between the needle tip and the collector surface was 15 cm. The drum collector was rotated about its axis at 34 rpm. The regenerated silk fibroin at the solution concentrations (8- 15 wt%) was electrospun onto the collector for 8 h. In examples, plates or other shaped collectors can be used as an alternative to a drum-shaped collector. In certain examples, a flat, wide supporting fabric, up to six-feet or more in examples, can be used as a collector with multiple needles in use as well. The size of the plate or planar substrate can influence the porosity of an electrospun film, or in some examples, other methods of controlling porosity as described herein can be used. In examples, a drum-shaped collector can have a diameter of from about 1 cm to about 15 cm, or from about 5 cm to about 10 cm, or from about 6 cm to about 9 cm. In other examples, the distance between the needle tip and the collector surface can be from about 1 cm to about 15 cm, or from about 5 cm to about 10 cm, or from about 6 cm to about 9 cm 15 cm. In examples, applied voltage should at least surpass a threshold voltage of about 1 kV/cm, or in examples, can be from about 1 kV/cm to

about 50 kV/cm, or from about 5 kV/cm to about 35 kV/cm, or from about 10 kV/cm to about 25 kV/cm. In examples, the collector may be stationary, while in some examples, the collector is in motion. For example, a drum or cylindrical collector can be in motion from about 20 rpm to about 45 rpm rpm, from about 5 rpm to about 100 rpm, or from about 20 to about 35 rpm. For electrospinning on laterally moving roll-to-roll base substrate (e.g., base fabric) for non-woven fabric manufacturing, the translational speed can range from about 1 m/min to about 50 m/min, or from about 5 m/min to about 40 m/min, or from about 10 m/min to about 25 m/min.

[0067] Optical and Structural Characterization: Transmissivity spectra of electrospun silk films were measured by a spectrophotometer (USB4000VIS-NIR, Ocean Optics) with an integrating sphere (ISP-50-8R, Ocean Optics). Nanostructures in electrospun silk films were characterized by scanning electron microscopy (SEM) (FEI, Helios Nanolab 660) after Au-Pd coating. Mean values and standard deviations in fiber diameters were calculated from measurements over 1100 – 1200 fibers based on the SEM images.

[0068] While the present teachings have been illustrated with respect to one or more implementations, alterations and/or modifications may be made to the illustrated examples without departing from the spirit and scope of the appended claims. For example, it may be appreciated that while the process is described as a series of acts or events, the present teachings are not limited by the ordering of such acts or events. Some acts may occur in different orders and/or concurrently with other acts or events apart from those described herein. Also, not all process stages may be required to implement a methodology in accordance with one or more aspects or embodiments of the present teachings. It may be appreciated that structural objects and/or processing stages may be added, or existing structural objects and/or processing stages may be removed or modified. Further, one or more of the acts depicted herein may be carried out in one or more separate acts and/or phases. Furthermore, to the extent that the terms "including," "includes," "having," "has," "with," or variants thereof are used in either the detailed description and the claims, such terms are intended to be inclusive in a manner similar to the term "comprising." The term "at least one of" is used to mean one or more of the listed items may be selected. Further, in the discussion and claims herein, the term "on" used with respect to two materials, one "on" the other, means at least some contact between the materials, while "over" means the materials are in proximity, but possibly with one or more additional intervening materials such that contact is possible but not required. Neither "on" nor "over" implies any directionality as used herein. The term "conformal" describes a coating material in which angles of the underlying material are preserved by the conformal material. The term "about" indicates that the value listed may be somewhat altered, as long as the alteration does not result in nonconformance of the process or structure to the illustrated embodiment. The terms "couple," "coupled," "connect,"

"connection," "connected," "in connection with," and "connecting" refer to "in direct connection with" or "in connection with via one or more intermediate elements or members." Finally, the terms "exemplary" or "illustrative" indicate the description is used as an example, rather than implying that it is an ideal. Other embodiments of the present teachings may be apparent to those skilled in the art from consideration of the specification and practice of the disclosure herein. It is intended that the specification and examples be considered as exemplary only, with a true scope and spirit of the present teachings being indicated by the following claims.

WHAT IS CLAIMED IS:

1. A method of generating a fibrous network film, the method comprising:

preparing a fibroin solution;

loading the fibroin solution into a syringe with a conductive needle or nozzle;

applying a high voltage to the needle or nozzle and grounding a conductive surface of a collector; and

electrospinning the fibroin solution from the syringe or nozzle with the conductive needle or nozzle to the grounded conductive surface of the collector to generate the fibrous network film on the grounded conductive surface.

2. The method of claim 1, wherein the collector moves in lateral motion relative to the conductive needle during the electrospinning.

3. The method of claim 2, wherein the collector is rotated.

4. The method of claim 1, wherein the conductive needle is a 21-gauge stainless-steel needle.

5. The method of claim 1, wherein the collector is drum-shaped with a diameter of about 1 cm to about 40 cm and the grounded conductive surface comprises stainless steel.

6. The method of claim 5, wherein the collector is rotated about an axis at of about 20 to about 45 rpm during the electrospinning.

7. The method of claim 1, wherein a distance between a tip of the conductive needle and the grounded conductive surface is 15 cm.

8. The method of claim 1, wherein the high voltage is approximately 21 kV.

9. The method of claim 1, wherein the preparing the fibroin solution comprises:

preparing a powder of regenerated silk fibroin; and

using the powder of regenerated silk fibroin to produce the fibroin solution.

10. The method of claim 9, wherein the preparing the powder of regenerated silk fibroin comprises:

removing sericin from white silk cocoons to produce degummed silk cocoons;

rinsing the degummed silk cocoons with distilled water at 100°C for 150 seconds;

further rinsing the rinsed degummed silk cocoons with cold distilled water;

drying the further rinsed degummed silk cocoons at 80°C for approximately 24 hours;

dissolving the dried silk cocoons at a liquor ratio of 1:20 in a CaCl2/H2O/EtOH (1/8/2 molar ratio) mixture solvent at 85 °C for approximately 30 minutes to produce a silk fibroin solution;

placing the silk fibroin solution in a tube of a cellulose membrane and dialyzing the silk fibroin solution for 4 days by circulating distilled water around the tube;

filtering the dialyzed silk fibroin solution through a polyethylene porous membrane to produce a filtered solution of regenerated silk fibroin;

drying the filtered solution of regenerated silk fibroin; and

grinding the dried, regenerated silk fibroin into the powder of regenerated silk fibroin.

11. The method of claim 10, wherein removing sericin from white silk cocoons to produce degummed silk cocoons comprises:

preparing an aqueous solution of 0.2% w/v sodium carbonate and 0.3% w/v sodium oleate;

heating the aqueous solution to 105°C; and

heating the white silk cocoons in the aqueous solution for approximately 90 minutes to produce the degummed silk cocoons.

12. The method of claim 10, wherein the white silk cocoons are Bombyx mori (Geumokjam) white silk cocoons.

13. The method of claim 10, wherein the cold distilled water is distilled water at approximately 10°C.

14. The method of claim 8, wherein using the regenerated silk fibroin powder to produce the fibroin solution comprises:

dissolving the regenerated silk fibroin powder in 98% formic acid for three hours at a concentration varying from 8 to 15 wt% to produce an unfiltered solution of silk fibroin; and

filtering the unfiltered solution of silk fibroin through a polyethylene porous membrane to produce the fibroin solution.

15. The fibrous network film generated by any of the method of claim 1.

16. An optical film comprising the fibrous network film of claim 15.

17. A clothing item comprising the fibrous network film of claim 15.

18. A method of generating a fibrous network film, the method comprising:

preparing a polymer solution;

loading the polymer solution into a syringe with a conductive needle;

applying a high voltage to the needle and grounding a conductive surface of a collector; and

electrospinning the polymer solution from the syringe with the conductive needle to the grounded conductive surface of the collector to generate the fibrous network film on the grounded conductive surface; and wherein:

an index of refraction of the fibrous network film is from about 1.4 to about 1.6; and

the fibrous network film comprises a plurality of electrospun polymer fibers.

19. A fibrous network film consisting of a plurality of electrospun fibers, wherein:

each of the plurality of electrospun fibers exhibits a fiber diameter value as a function of fiber length such that a relative standard deviation σ of fiber diameter values for each of the plurality of electrospun fibers is approximately 0.32;

the plurality of electrospun fibers, taken together, exhibit a mean fiber diameter value that is one of: approximately 0.30 μm and approximately 0.32 μm; and

the plurality of electrospun fibers in the fibrous network film exhibit a filling fraction from approximately 10% to approximately 60%.

20. The fibrous network film of claim 19 wherein the filling fraction is between approximately 31% and approximately 45%.

21. The fibrous network film of claim 20 wherein the mean fiber diameter value is approximately 0.32 μm and the filling fraction is approximately 38%.

22. A fibrous network film consisting of a plurality of electrospun fibers, wherein:

each of the plurality of electrospun fibers exhibits a fiber diameter value as a function of fiber length such that a relative standard deviation σ of fiber diameter values for each of the plurality of electrospun fibers is approximately 0.35;

the plurality of electrospun fibers, taken together, exhibit a mean fiber diameter value that is approximately 0.20 μm; and

the plurality of electrospun fibers in the fibrous network film exhibit a filling fraction from approximately 10% to approximately 60%.

23. The fibrous network film of claim 22 wherein the filling fraction is between approximately 31% and approximately 45%.

24. The fibrous network film generated by the method of claim 1, wherein:

the electrospinning the fibroin solution from the syringe with the conductive needle to the grounded conductive surface of the collector to generate the fibrous network film on the grounded conductive surface comprises generating a plurality of electrospun fibers; wherein

each of the plurality of electrospun fibers exhibits a fiber diameter value as a function of fiber length such that a relative standard deviation σ of fiber diameter values for each of the plurality of electrospun fibers is approximately 0.32;

the plurality of electrospun fibers, taken together, exhibit a mean fiber diameter value that is one of: approximately 0.30 μm and approximately 0.32 μm; and

the plurality of electrospun fibers in the fibrous network film exhibit a filling fraction from approximately 10% to approximately 60%.

25. The fibrous network film of claim 24 wherein the filling fraction is between approximately 31% and approximately 45%.

26. The fibrous network film of claim 25 wherein the mean fiber diameter value is approximately 0.32 μm and the filling fraction is approximately 38%.

27. The fibrous network film generated by the method of claim 1, wherein:

the electrospinning the fibroin solution from the syringe with the conductive needle to the grounded conductive surface of the collector to generate the fibrous network film on the grounded conductive surface comprises generating a plurality of electrospun fibers; wherein

each of the plurality of electrospun fibers exhibits a fiber diameter value as a function of fiber length such that a relative standard deviation σ of fiber diameter values for each of the plurality of electrospun fibers is approximately 0.35;

the plurality of electrospun fibers, taken together, exhibit a mean fiber diameter value that is approximately 0.20 μm; and

the plurality of electrospun fibers in the fibrous network film exhibit a filling fraction from approximately 10% to approximately 60%.

28. The fibrous network film of claim 26, wherein the filling fraction is between approximately 31% and approximately 45%.

29. The fibrous network film of claim 26, wherein an index of refraction of the fibrous network film is from about 1.4 to about 1.6.

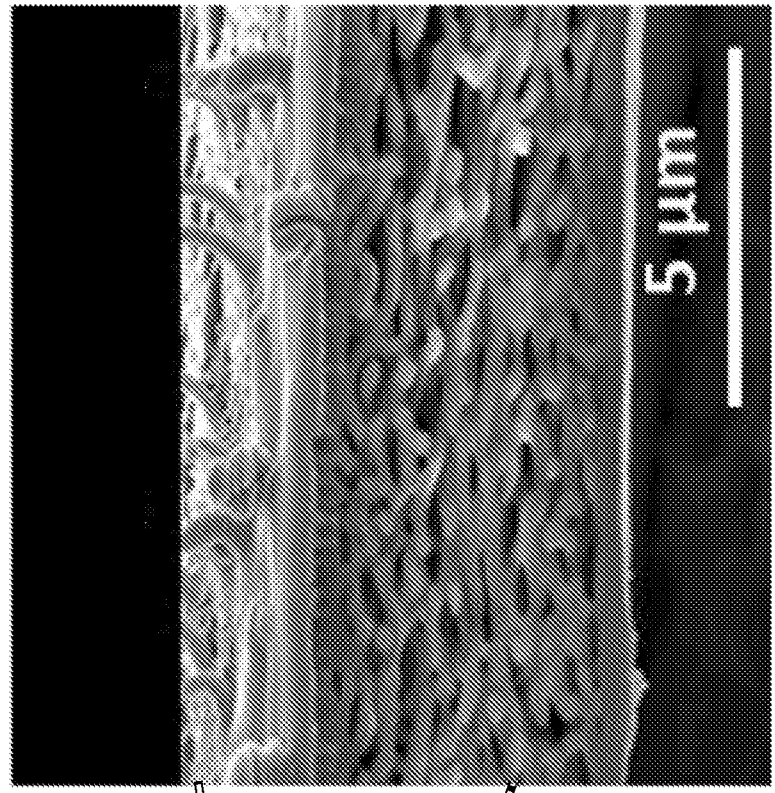

FIG. 1B

FIG. 1A

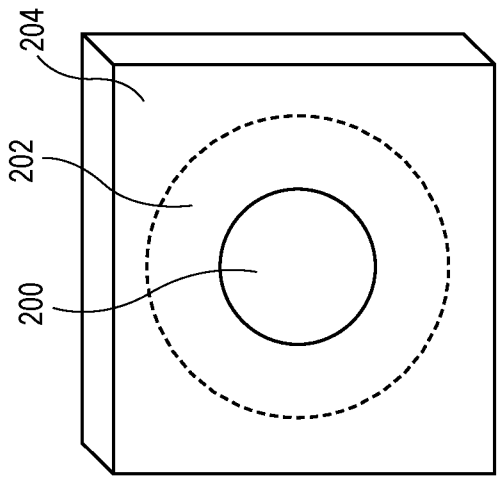

FIG. 2A

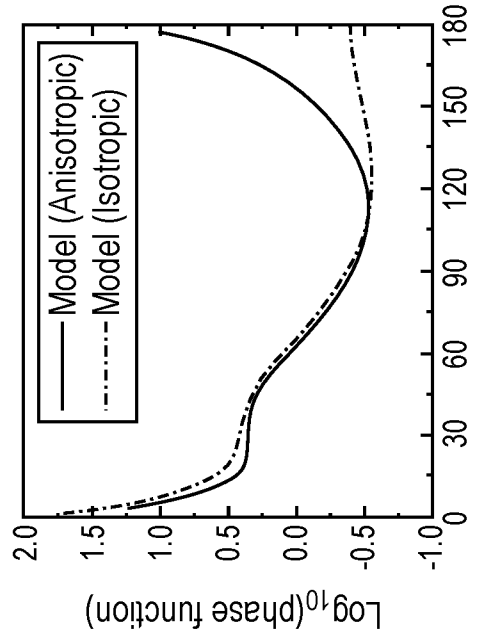

FIG. 2B

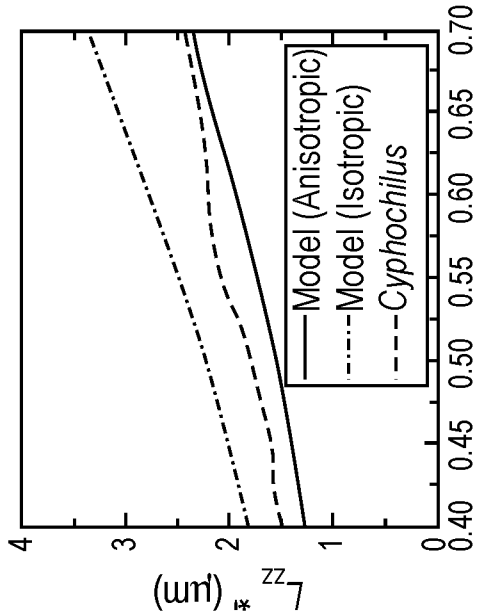

FIG. 2C

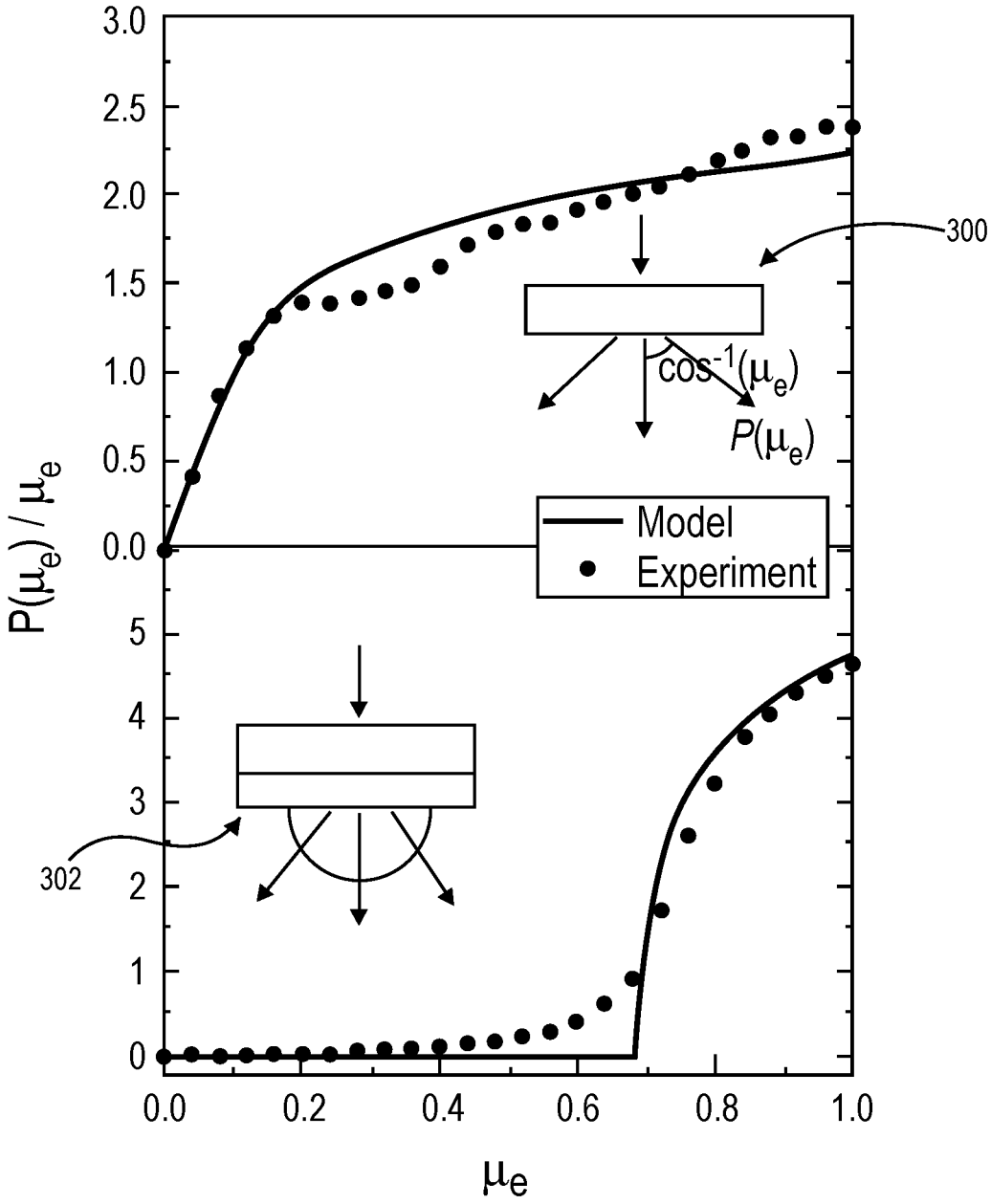
3.0
2.5
2.0
1.5
1.0
0.5
0.0
5
4
3
2
1
0
0.0
0.2
0.4
0.6
0.8
1.0
P(μe) / μe
μe
300
302
cos-1(μe)
P(μe)
Model
Experiment

FIG. 3

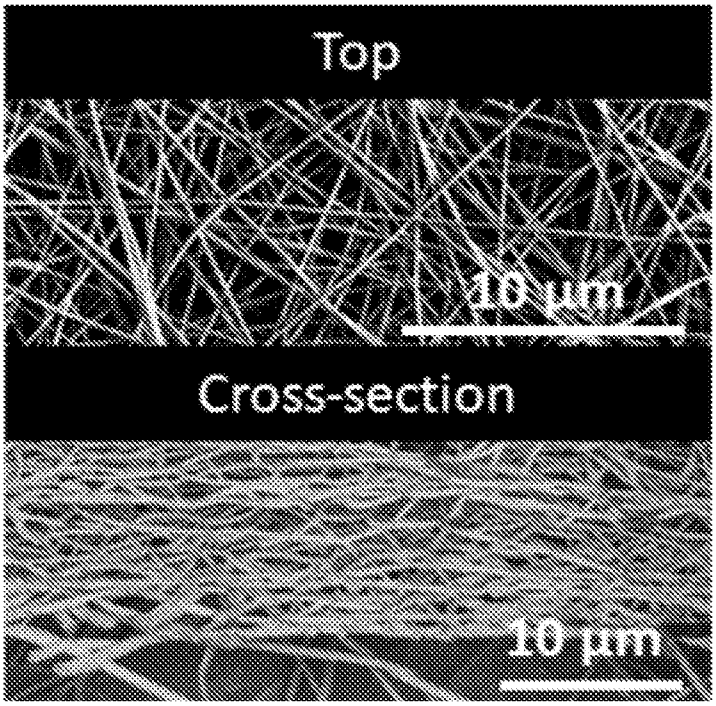
Top
10 µm
Cross-section
10 µm

FIG. 4A

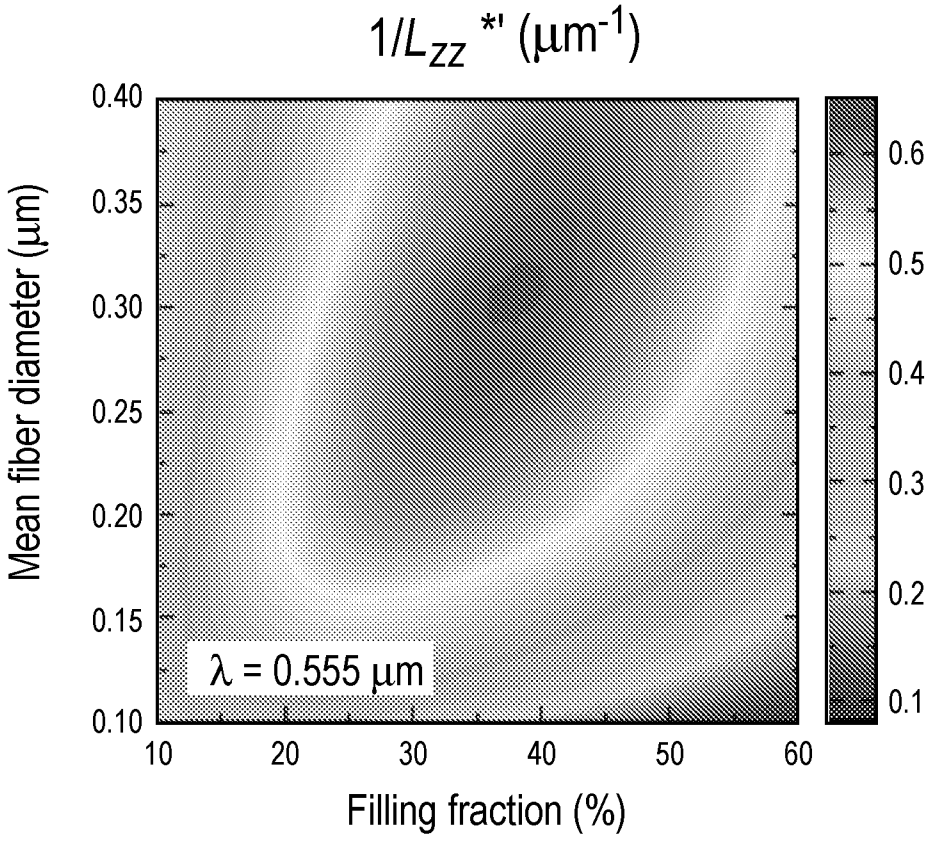
1/L_zz *' (µm^-1)
Mean fiber diameter (µm)
0.40
0.35
0.30
0.25
0.20
0.15
0.10
λ = 0.555 µm
10
20
30
40
50
60
Filling fraction (%)
0.6
0.5
0.4
0.3
0.2
0.1

FIG. 4B

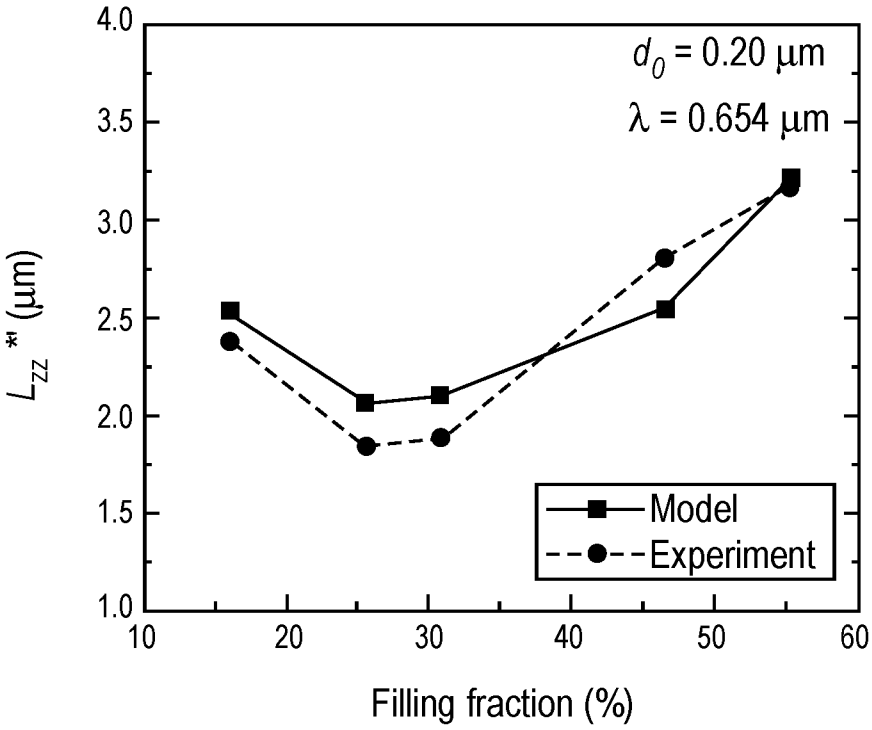
d_0 = 0.20 μm
λ = 0.654 μm
L_{zz}*' (μm)
Model
Experiment
Filling fraction (%)
4.0
3.5
3.0
2.5
2.0
1.5
1.0
10
20
30
40
50
60

FIG. 4C

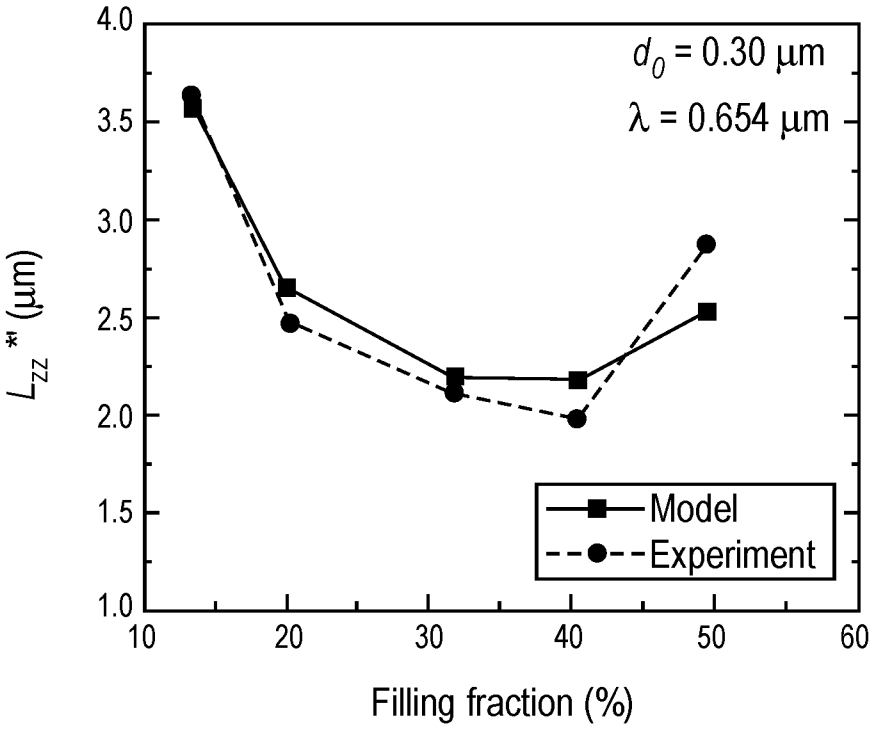
d_0 = 0.30 μm
λ = 0.654 μm
L_{zz}*' (μm)
Model
Experiment
Filling fraction (%)
4.0
3.5
3.0
2.5
2.0
1.5
1.0
10
20
30
40
50
60

FIG. 4D

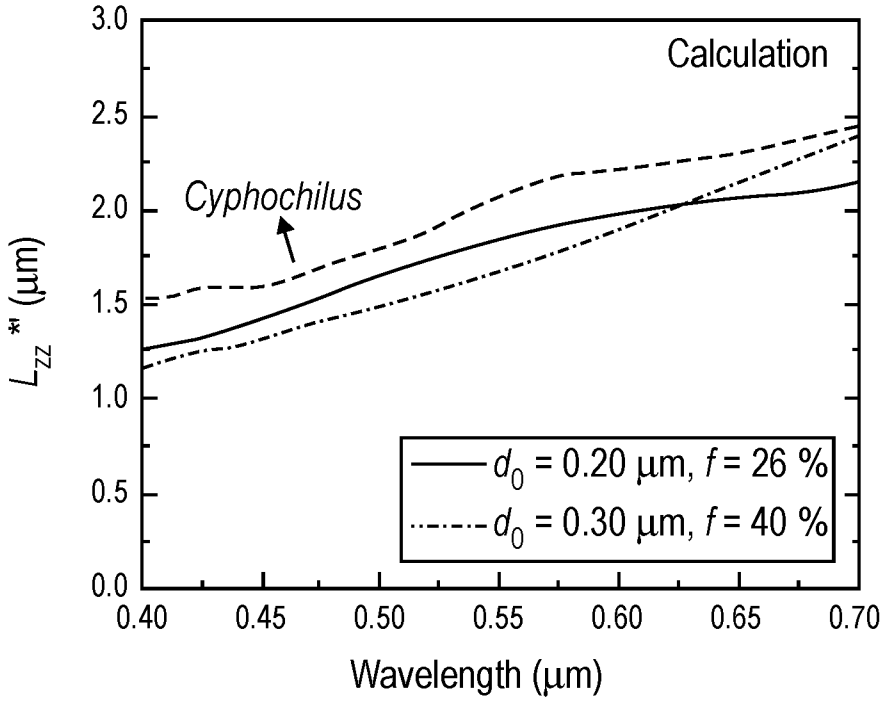
Calculation
Cyphochilus
L_{ZZ}* (μm)
d_0 = 0.20 μm, f = 26 %
d_0 = 0.30 μm, f = 40 %
Wavelength (μm)
3.0
2.5
2.0
1.5
1.0
0.5
0.0
0.40
0.45
0.50
0.55
0.60
0.65
0.70

FIG. 4E

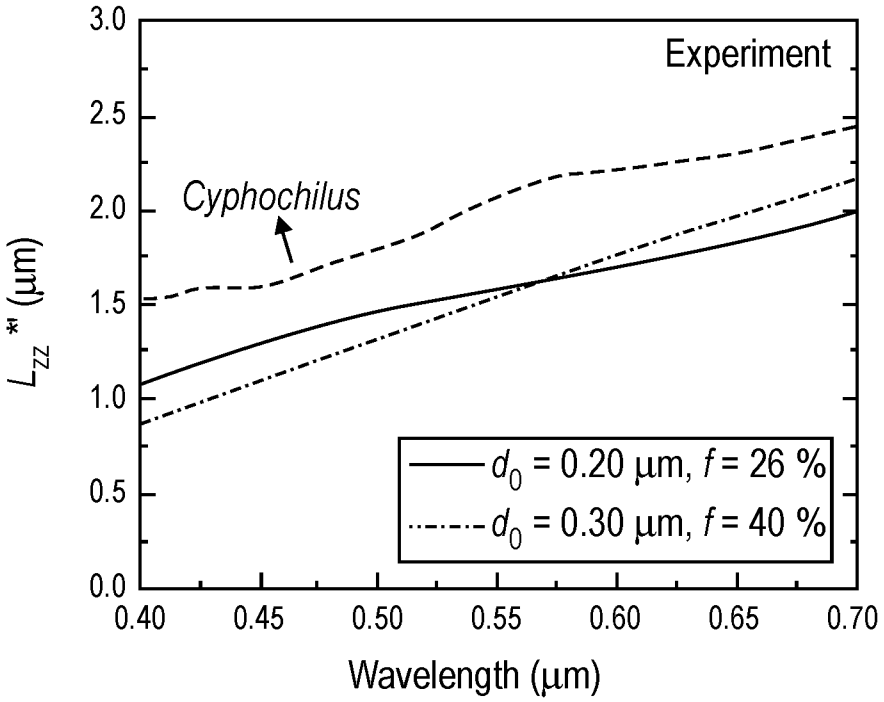
Experiment
Cyphochilus
L_{ZZ}* (μm)
d_0 = 0.20 μm, f = 26 %
d_0 = 0.30 μm, f = 40 %
Wavelength (μm)
3.0
2.5
2.0
1.5
1.0
0.5
0.0
0.40
0.45
0.50
0.55
0.60
0.65
0.70

FIG. 4F

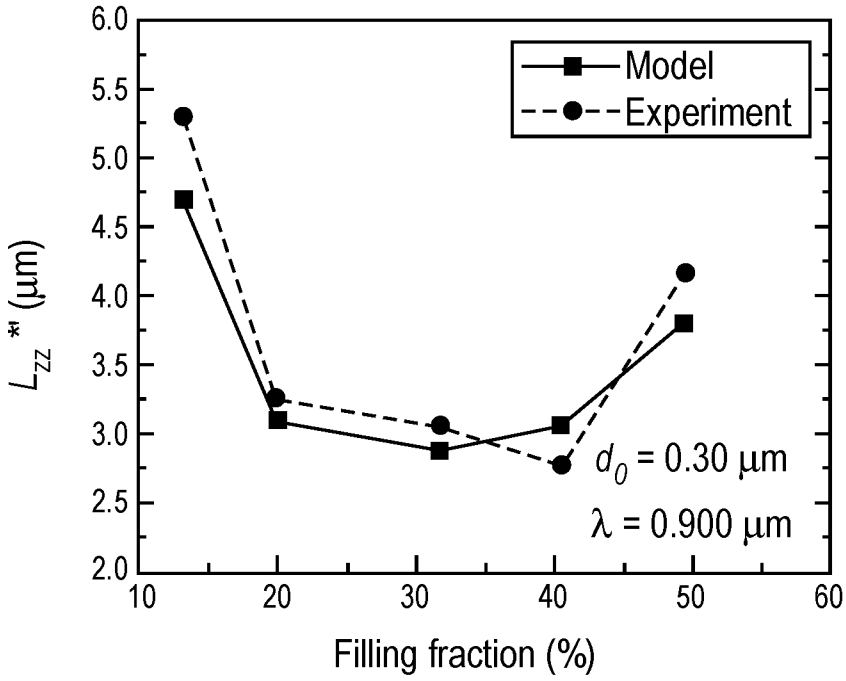
Model
Experiment
d_0 = 0.30 μm
λ = 0.900 μm
L_{zz}* (μm)
Filling fraction (%)
6.0
5.5
5.0
4.5
4.0
3.5
3.0
2.5
2.0
10
20
30
40
50
60

FIG. 5A

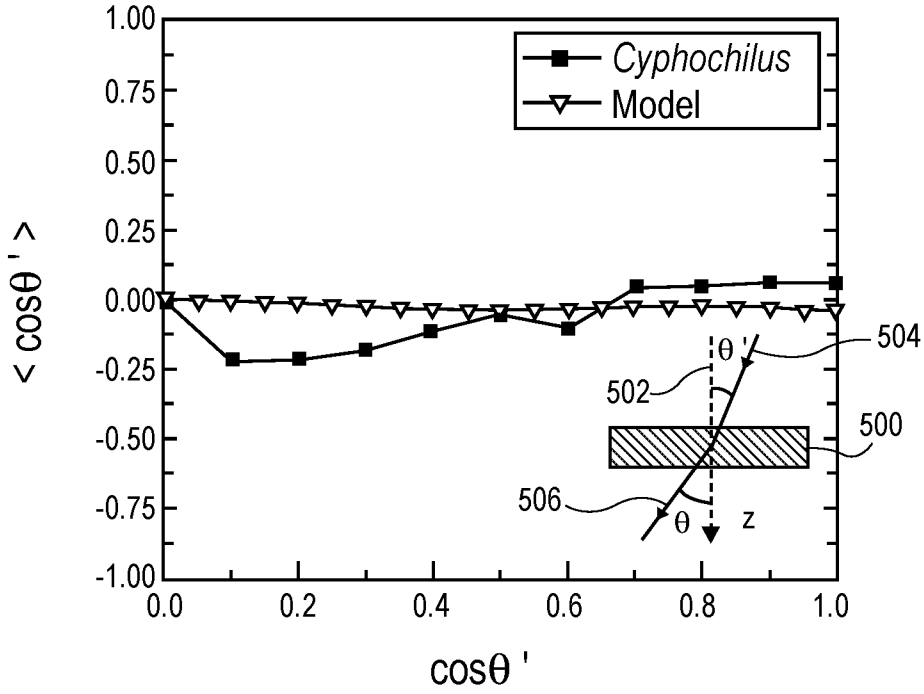
Cyphochilus
Model
< cosθ ' >
cosθ '
θ '
504
502
500
506
θ
z
1.00
0.75
0.50
0.25
0.00
-0.25
-0.50
-0.75
-1.00
0.0
0.2
0.4
0.6
0.8
1.0

FIG. 5B

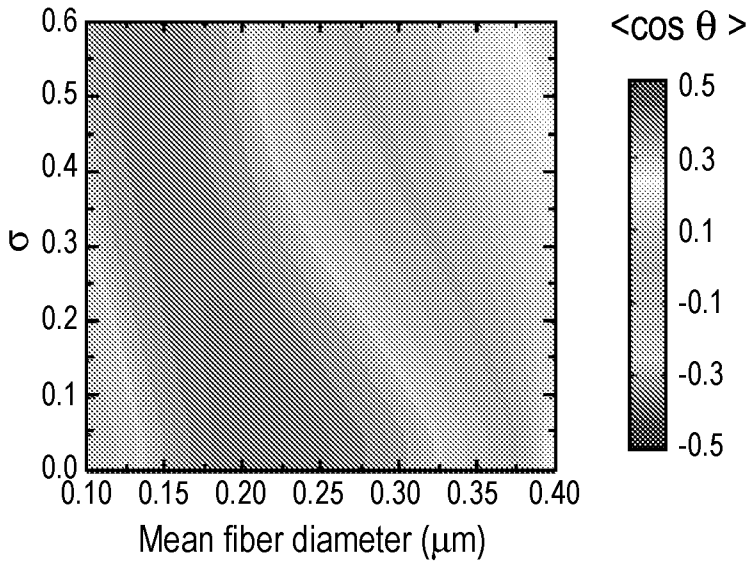

FIG. 6A

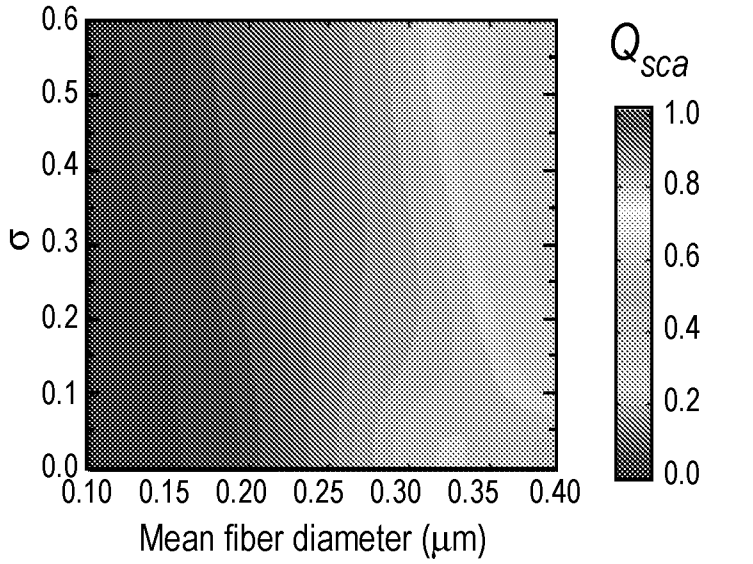

FIG. 6B

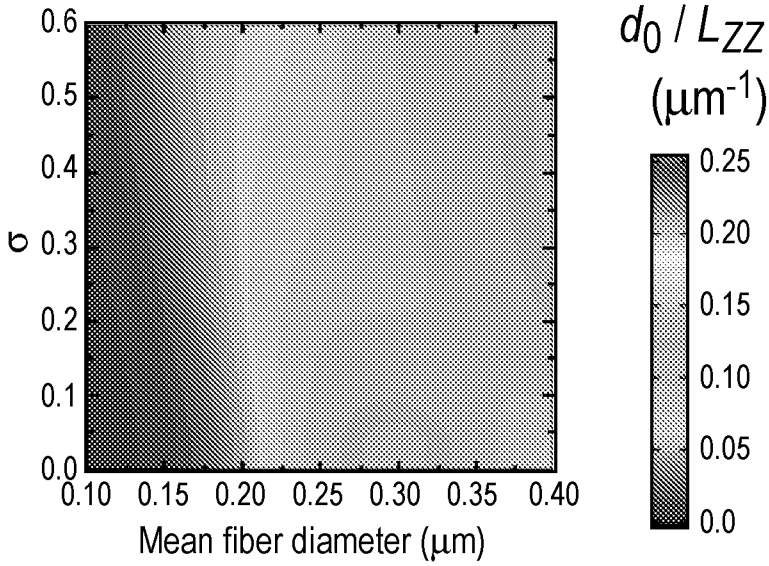

FIG. 6C

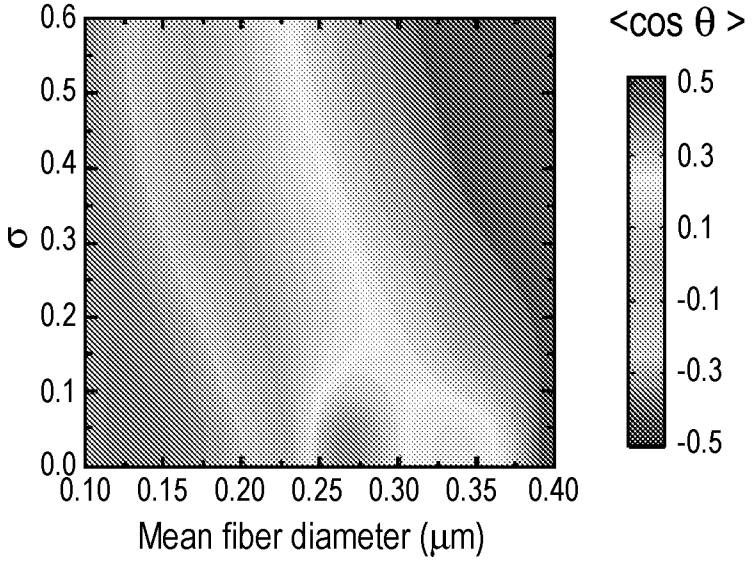

FIG. 6D

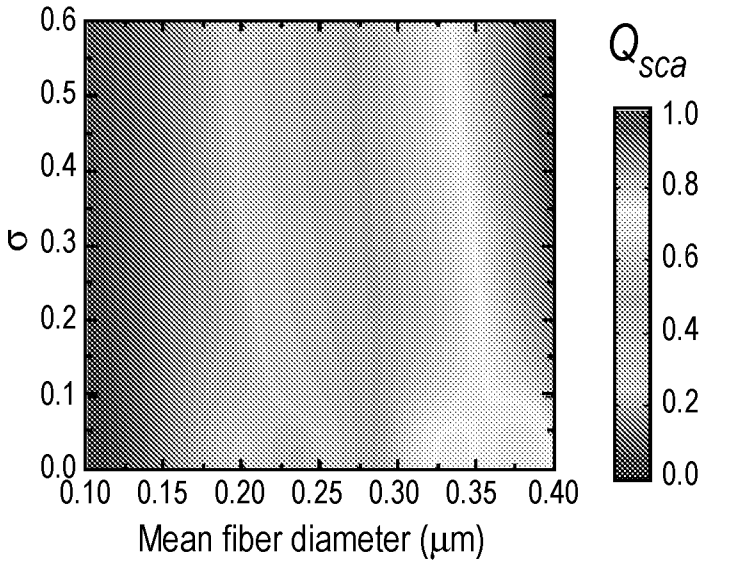

FIG. 6E

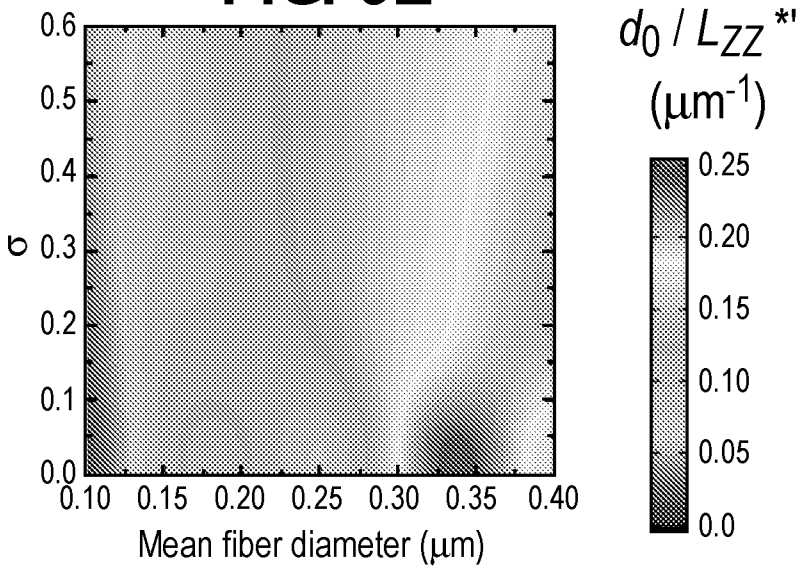

FIG. 6F

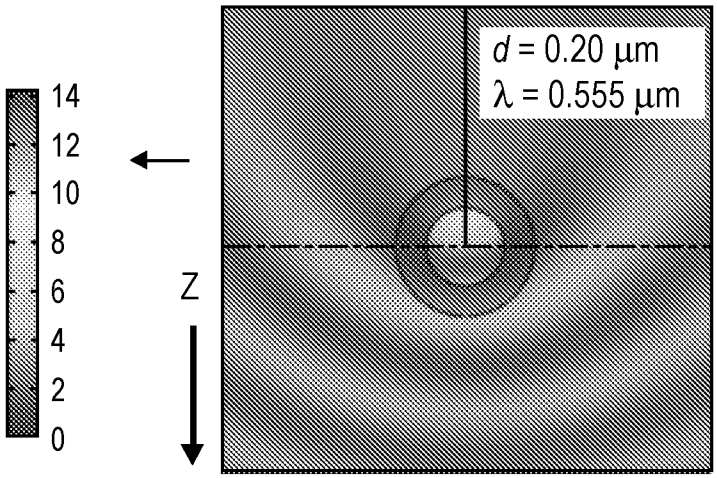

FIG. 6G

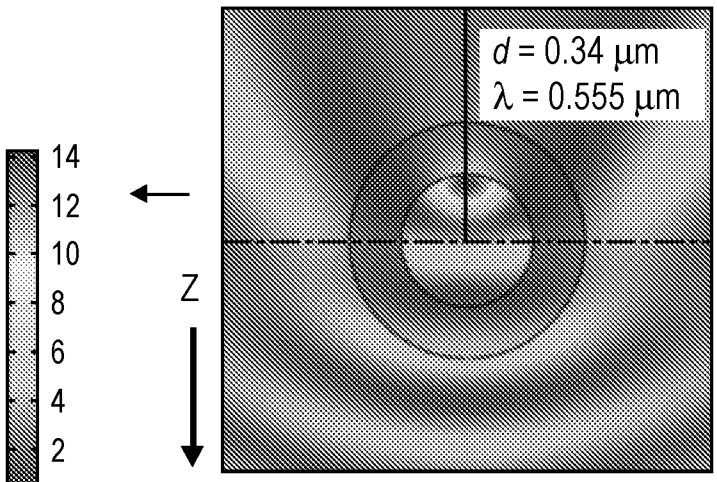

FIG. 6H

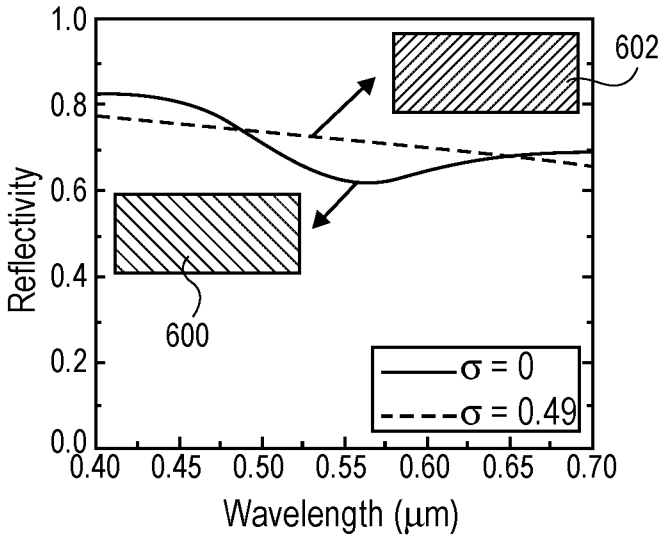

FIG. 6I

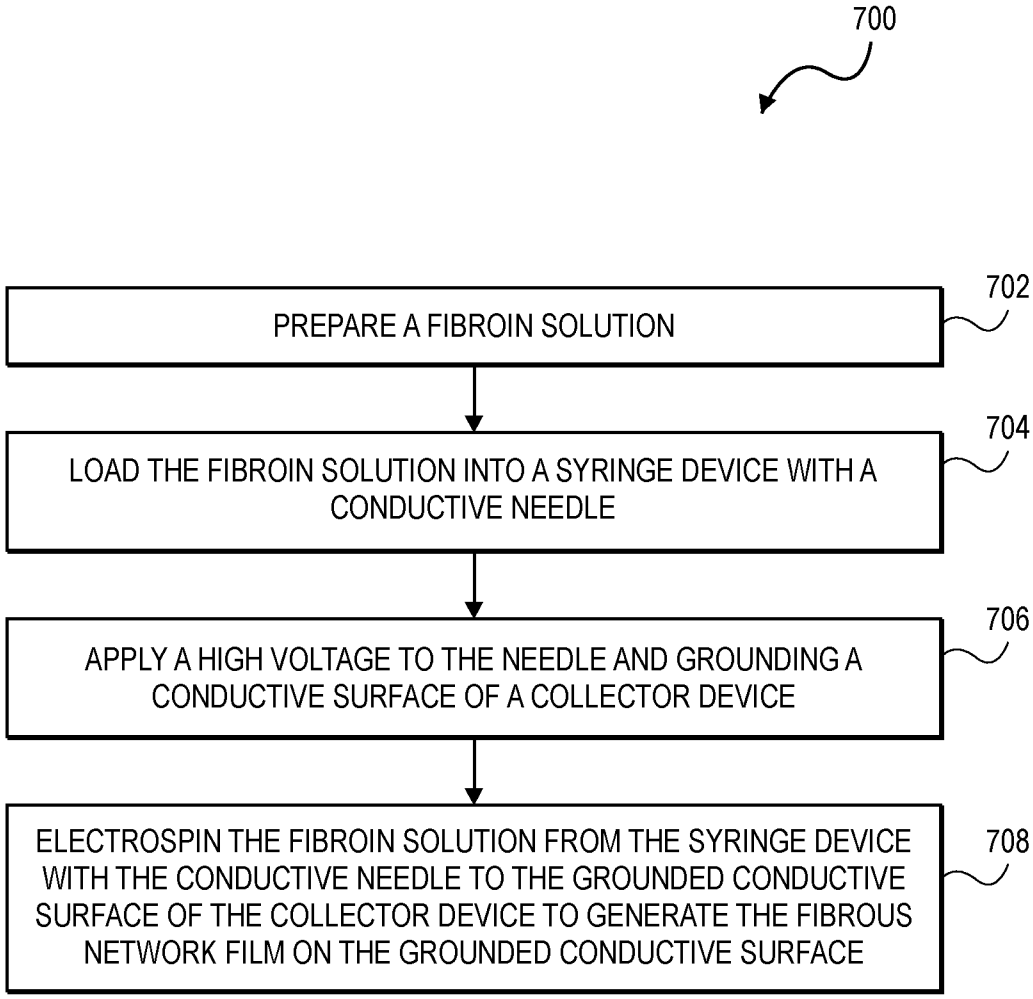
700
PREPARE A FIBROIN SOLUTION
702
LOAD THE FIBROIN SOLUTION INTO A SYRINGE DEVICE WITH A CONDUCTIVE NEEDLE
704
APPLY A HIGH VOLTAGE TO THE NEEDLE AND GROUNDING A CONDUCTIVE SURFACE OF A COLLECTOR DEVICE
706
ELECTROSPIN THE FIBROIN SOLUTION FROM THE SYRINGE DEVICE WITH THE CONDUCTIVE NEEDLE TO THE GROUNDED CONDUCTIVE SURFACE OF THE COLLECTOR DEVICE TO GENERATE THE FIBROUS NETWORK FILM ON THE GROUNDED CONDUCTIVE SURFACE
708

FIG. 7

INTERNATIONAL SEARCH REPORT

International application No.
PCT/US2023/065431

A. CLASSIFICATION OF SUBJECT MATTER

D04H 3/015(2012.01)i; **D01D 5/00**(2006.01)i; **D01B 7/02**(2006.01)i; **D01C 3/00**(2006.01)i; **D04H 3/16**(2006.01)i

According to International Patent Classification (IPC) or to both national classification and IPC

B. FIELDS SEARCHED

Minimum documentation searched (classification system followed by classification symbols)

D04H 3/015(2012.01); A61F 2/02(2006.01); A61L 27/20(2006.01); B82B 3/00(2006.01); C07K 14/435(2006.01); C07K 14/50(2006.01); C12N 5/02(2006.01); D01D 5/00(2006.01); D01D 5/06(2006.01); G01N 33/32(2006.01)

Documentation searched other than minimum documentation to the extent that such documents are included in the fields searched

Korean utility models and applications for utility models
Japanese utility models and applications for utility models

Electronic data base consulted during the international search (name of data base and, where practicable, search terms used)

eKOMPASS(KIPO internal) & Keywords: fibroin, solution, electrospinning, syringe, needle, collector, film

C. DOCUMENTS CONSIDERED TO BE RELEVANT

Category*	Citation of document, with indication, where appropriate, of the relevant passages	Relevant to claim No.
X	WO 2021-081393 A1 (UNM RAINFOREST INNOVATIONS) 29 April 2021 (2021-04-29) claims 20, 21; paragraphs [0040]-[0045]	1-29
A	WO 2010-102533 A1 (MEDPRIN REGENERATIVE MEDICAL TECHNOLOGIES CO., LTD.) 16 September 2010 (2010-09-16) the whole document	1-29
A	WO 2021-102523 A1 (ROYAL MELBOURNE INSTITUTE OF TECHNOLOGY) 03 June 2021 (2021-06-03) the whole document	1-29
A	EP 3412682 A1 (TRUSTEES OF TUFTS COLLEGE) 12 December 2018 (2018-12-12) the whole document	1-29
A	WO 2011-068389 A2 (AMOGREENTECH CO., LTD.) 09 June 2011 (2011-06-09) the whole document	1-29

☐ Further documents are listed in the continuation of Box C. ☑ See patent family annex.

* Special categories of cited documents:
"A" document defining the general state of the art which is not considered to be of particular relevance
"D" document cited by the applicant in the international application
"E" earlier application or patent but published on or after the international filing date
"L" document which may throw doubts on priority claim(s) or which is cited to establish the publication date of another citation or other special reason (as specified)
"O" document referring to an oral disclosure, use, exhibition or other means
"P" document published prior to the international filing date but later than the priority date claimed
"T" later document published after the international filing date or priority date and not in conflict with the application but cited to understand the principle or theory underlying the invention
"X" document of particular relevance; the claimed invention cannot be considered novel or cannot be considered to involve an inventive step when the document is taken alone
"Y" document of particular relevance; the claimed invention cannot be considered to involve an inventive step when the document is combined with one or more other such documents, such combination being obvious to a person skilled in the art
"&" document member of the same patent family

Date of the actual completion of the international search	Date of mailing of the international search report
25 July 2023	**25 July 2023**

Name and mailing address of the ISA/KR	Authorized officer
Korean Intellectual Property Office **189 Cheongsa-ro, Seo-gu, Daejeon** **35208, Republic of Korea**	**KIM, Tae Woon**
Facsimile No. **+82-42-481-8578**	Telephone No. **+82-42-481-5003**

INTERNATIONAL SEARCH REPORT
Information on patent family members

International application No.
PCT/US2023/065431

Patent document cited in search report	Publication date (day/month/year)	Patent family member(s)	Publication date (day/month/year)
WO 2021-081393 A1	29 April 2021	US 2022-365512 A1	17 November 2022
WO 2010-102533 A1	16 September 2010	BR PI1006250 A2	04 June 2019
		BR PI1006250 B1	10 December 2019
		CN 101507661 A	19 August 2009
		CN 101507661 B	10 November 2010
		CN 101559242 A	21 October 2009
		CN 101559242 B	29 July 2015
		CN 101692986 A	14 April 2010
		CN 101692986 B	18 May 2011
		EP 2340785 A1	06 July 2011
		EP 2340785 A4	03 April 2013
		EP 2340785 B1	18 May 2016
		JP 2012-519559 A	30 August 2012
		JP 5658175 B2	21 January 2015
		KR 10-2011-0133599 A	13 December 2011
		KR 10-2014-0090704 A	17 July 2014
		MX 2011009282 A	28 October 2011
		MX 345863 B	20 February 2017
		MX 345864 B	20 February 2017
		RU 2011140225 A	20 April 2013
		RU 2491961 C2	10 September 2013
		US 2012-0029654 A1	02 February 2012
		US 2014-0205647 A1	24 July 2014
		US 2014-0222163 A1	07 August 2014
		US 8795708 B2	05 August 2014
		US 9211180 B2	15 December 2015
		US 9271822 B2	01 March 2016
WO 2021-102523 A1	03 June 2021	AU 2020-390759 A1	16 June 2022
		AU 2020-390759 A8	23 June 2022
		CA 3166443 A1	03 June 2021
		CN 115315411 A	08 November 2022
		EP 4065511 A1	05 October 2022
		KR 10-2022-0143001 A	24 October 2022
		US 2023-0012274 A1	12 January 2023
EP 3412682 A1	12 December 2018	CN 105593773 A	18 May 2016
		CN 105593773 B	05 April 2019
		EP 2970411 A2	20 January 2016
		EP 2970411 B1	09 May 2018
		EP 3412682 B1	31 August 2022
		EP 4180448 A1	17 May 2023
		ES 2935659 T3	09 March 2023
		GB 2536810 A	28 September 2016
		GB 2536810 B	28 October 2020
		JP 2016-517443 A	16 June 2016
		JP 2016-541037 A	28 December 2016
		JP 2018-168198 A	01 November 2018
		JP 2021-080277 A	27 May 2021
		JP 6437535 B2	12 December 2018
		JP 6457482 B2	23 January 2019
		JP 7257112 B2	13 April 2023

INTERNATIONAL SEARCH REPORT
Information on patent family members

International application No.
PCT/US2023/065431

Patent document cited in search report	Publication date (day/month/year)	Patent family member(s)	Publication date (day/month/year)
		KR 10-2015-0131329 A	24 November 2015
		KR 10-2021-0149207 A	08 December 2021
		KR 10-2023-0021768 A	14 February 2023
		KR 10-2457668 B1	21 October 2022
		US 10432456 B2	01 October 2019
		US 11376329 B2	05 July 2022
		US 2015-0095788 A1	02 April 2015
		US 2016-0046679 A1	18 February 2016
		US 2016-0237128 A1	18 August 2016
		US 2016-0263228 A1	15 September 2016
		US 2020-0165306 A1	28 May 2020
		US 2021-0002335 A1	07 January 2021
		WO 2014-145002 A2	18 September 2014
		WO 2014-145002 A3	29 January 2015
		WO 2015-048384 A1	02 April 2015
		WO 2015-048527 A1	02 April 2015
WO 2011-068389 A2	09 June 2011	KR 10-1313156 B1	30 September 2013
		KR 10-2011-0063375 A	10 June 2011
		KR 10-2011-0063390 A	10 June 2011
		WO 2011-068389 A3	10 November 2011